ACSNANO

www.acsnano.org

ARTICLE

Stealth Effect of Short Polyoxazolines in Graft Copolymers: Minor Changes of Backbone End Group Determine Liver Cell-Type Specificity

Irina Muljajew, Sophie Huschke, Anuradha Ramoji, Zoltán Cseresnyés, Stephanie Hoeppener, Ivo Nischang, Wanling Foo, Jürgen Popp, Marc Thilo Figge, Christine Weber, Michael Bauer, Ulrich S. Schubert,* and Adrian T. Press*

Cite This: *ACS Nano* 2021, 15, 12298–12313

Read Online

ACCESS | Metrics & More | Article Recommendations | Supporting Information

ABSTRACT: **Dye-loaded micelles of 10 nm diameter formed from amphiphilic graft copolymers composed of a hydrophobic poly(methyl methacrylate) backbone and hydrophilic poly(2-ethyl-2-oxazoline) side chains with a degree of polymerization of 15 were investigated concerning their cellular interaction and uptake *in vitro* as well as their interaction with local and circulating cells of the reticuloendothelial system in the liver by intravital microscopy. Despite the high molar mass of the individual macromolecules ($M_n \approx 20$ kg mol^{-1}), backbone end group modification by attachment of a hydrophilic anionic fluorescent probe strongly affected the *in vivo* performance. To understand these effects, the end group was additionally modified by the attachment of four methacrylic acid repeating units. Although various micelles appeared similar in dynamic light scattering and cryo-transmission electron microscopy, changes in the micelles were evident from principal component analysis of the Raman spectra. Whereas an efficient stealth effect was found for micelles formed from polymers with anionically charged or thiol end groups, a hydrophobic end group altered the micelles' structure sufficiently to adapt cell-type specificity and stealth properties in the liver.**

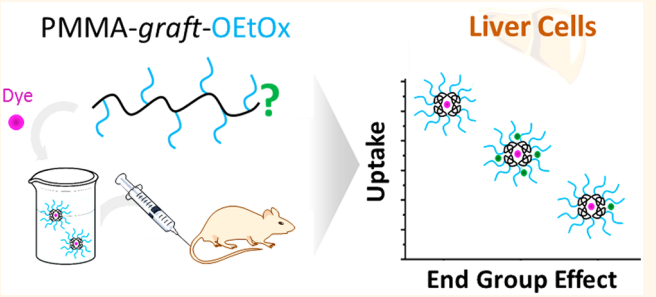

KEYWORDS: *polyoxazoline, graft copolymer, micelle, drug delivery, liver, reticuloendothelial system, intravital microscopy*

INTRODUCTION

Targeting drugs to a desired tissue or cell-type is a common goal of modern pharmaceutical approaches. Often, carriers are used which employ active, passive, or a combination of both targeting strategies to enrich their payload in the desired environment.[1] For the encapsulation and the controlled release of numerous small molecules, polymeric drug carrier systems represent attractive vehicles for tissue-specific drug delivery.[2] Nanocarriers such as micelles below 50 nm in diameter were reported to be preferable in the use of tumor treatment.[3] Their small size leads to favorable tissue penetration properties, which allows them to reach even poorly perfused tissue, *e.g.*, hypoxic tumor areas. Their small size further leads to rapid renal filtration and elimination. The resulting short circulation time decreases the risk for nonspecific uptake and detrimental side effects. Since polymer-based nanoparticles are foreign bodies for the host, the reticuloendothelial system (RES) recognizes, engulfs, and destroys them.[4] In the worst case, the RES additionally triggers an inflammatory response which decreases the effectiveness of further nanoparticle-based drug applications due to the generation of specific antibodies against these carriers.[5]

The coupling of stealth polymers to polymeric drug carriers can prevent their recognition by the RES and thereby decreases unspecific side effects and also the necessary amount of polymer-encapsulated drug to be administered.[6] The current clinical standard for stealth polymers used in many drug formulations is poly(ethylene glycol) (PEG).[7−9] It is successfully applied in various drug formulations to solubilize hydrophobic compounds for systemic administration or as stealth polymer for nanoparticles.[10] Moreover, it is also commonly used in food and daily cosmetic products. The consequences of such often long-term exposures are subclinical

Received: May 18, 2021
Accepted: June 28, 2021
Published: July 16, 2021

https://doi.org/10.1021/acsnano.1c04213
ACS Nano 2021, 15, 12298−12313

Scheme 1. Schematic Representation of the Synthesis Route toward the PMMA-*graft*-OEtOx$_{15}$ Graft Copolymers P5, P5-SH, P5-DY654, and P5-MAA$_4$[a]

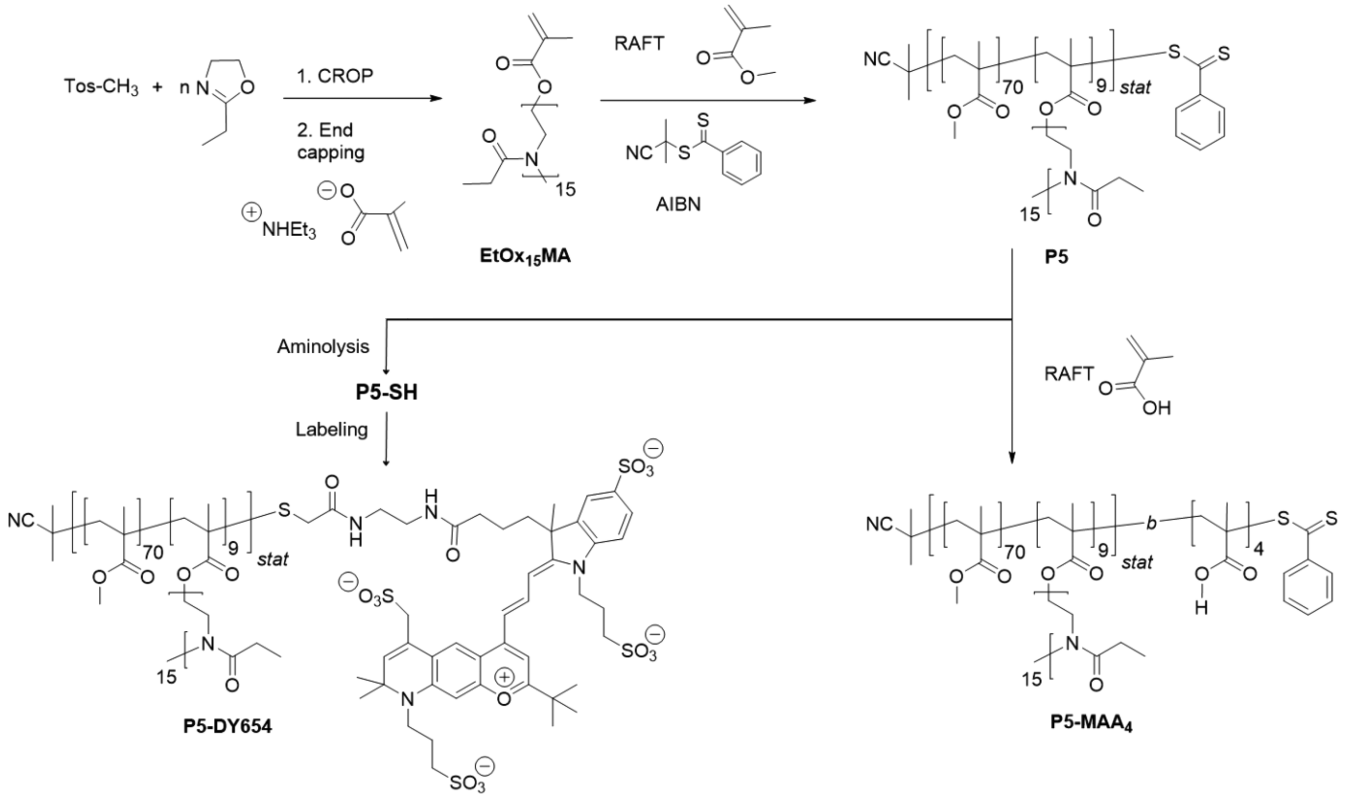

[a]CROP: Cationic ring-opening polymerization. RAFT: Reversible addition−fragmentation chain transfer polymerization. AIBN: 2,2′-Azobis(2-methylpropionitrile).

immune reactions, resulting in the production of anti-PEG antibodies in individuals. Studies on healthy individuals from 2016 confirmed detectable levels of anti-PEG antibodies in up to 72% of the tested individuals, which had not been in contact with PEG-containing clinical drugs.[11−13] These antibodies can render PEG-mediated stealth effects of drug carriers ineffective by recognizing and binding PEG on the surface of these drug carriers, marking them for immune cells. The induction of the immune system further may trigger mild to severe side effects, resulting in intolerance reactions as severe as anaphylaxis.[13] Therefore, alternative stealth polymers were introduced in the past few years.

A promising candidate to overcome bottlenecks of clinical translation is poly(2-ethyl-2-oxazoline) (PEtOx).[14] Kierstead *et al.* investigated the induction of accelerated blood clearance with liposomes modified with various potential stealth polymers, including poly(2-methyl-2-oxazoline) (PMeOx).[15] In this mentioned study, PEG and PMeOx were both rapidly cleared, whereas poly(*N*-vinyl-2-pyrrolidone), poly(*N*,*N*-dimethylacrylamide), poly{*N*-(2-hydroxypropyl)methacrylamide}, and poly(*N*-acryloylmorpholine) modifications did not cause accelerated blood clearance in rats. However, in the same species, Woodle *et al.* investigated PMeOx- and PEtOx-based lipid conjugates and found a long circulation time.[16] In line with these findings, Moreadith *et al.* did not observe antibody formation against PEtOx in rabbits, suggesting stealth properties of PEtOx.[17] In fact, PEtOx−drug conjugates directed against Parkinson's disease and restless leg syndrome have reached Phase 2 clinical trials.[18] In addition to the covalent attachment of PEtOx to active pharmaceutical ingredients, hydrophilic poly(2-oxazoline)s (POx), such as PEtOx, form part of various drug delivery vehicles such as micelles, polyplexes, or nanoparticles in academic research.[19,20] In particular for micellar drug carriers, PEtOx is mostly introduced as part of linear block copolymers in combination with hydrophobic blocks. Although the variation of the amphiphilic di- or triblock copolymer architecture may lead to differently assembled structures depending on the length of the hydrophilic block,[21] the use of branched structures may contribute to overcoming dissociation issues.[22] Exploiting other polymer architectures, such as amphiphilic graft copolymers, can hence be attractive for the design of drug delivery systems. For instance, graft copolymers composed of polyesters and PEG reduced the protein adsorption compared to their linear block copolymer analogues, thereby demonstrating improved stealth properties.[23,24]

Graft copolymers with hydrophobic polytyrosine[25] or polycaprolactone[26] backbones and hydrophilic POx side chains and heterografted comb polymers comprising PLA and PEtOx side chains[27] are capable of self-assembly and of encapsulating hydrophobic dyes. For instance, the micellization of poly(2-nitrobenzyl acrylate) as a hydrophobic building block and PEtOx was more straightforward in a graft copolymer architecture than that of the linear block copolymer.[28,29] Also, more complex systems comprising coumarin moieties revealed micellization and enabled the encapsulation of a hydrophobic photosensitizer.[30,31] However, to the best of our knowledge, the *in vivo* performance of POx-based graft copolymer micelles has not been reported so far.

https://doi.org/10.1021/acsnano.1c04213
ACS Nano 2021, 15, 12298−12313

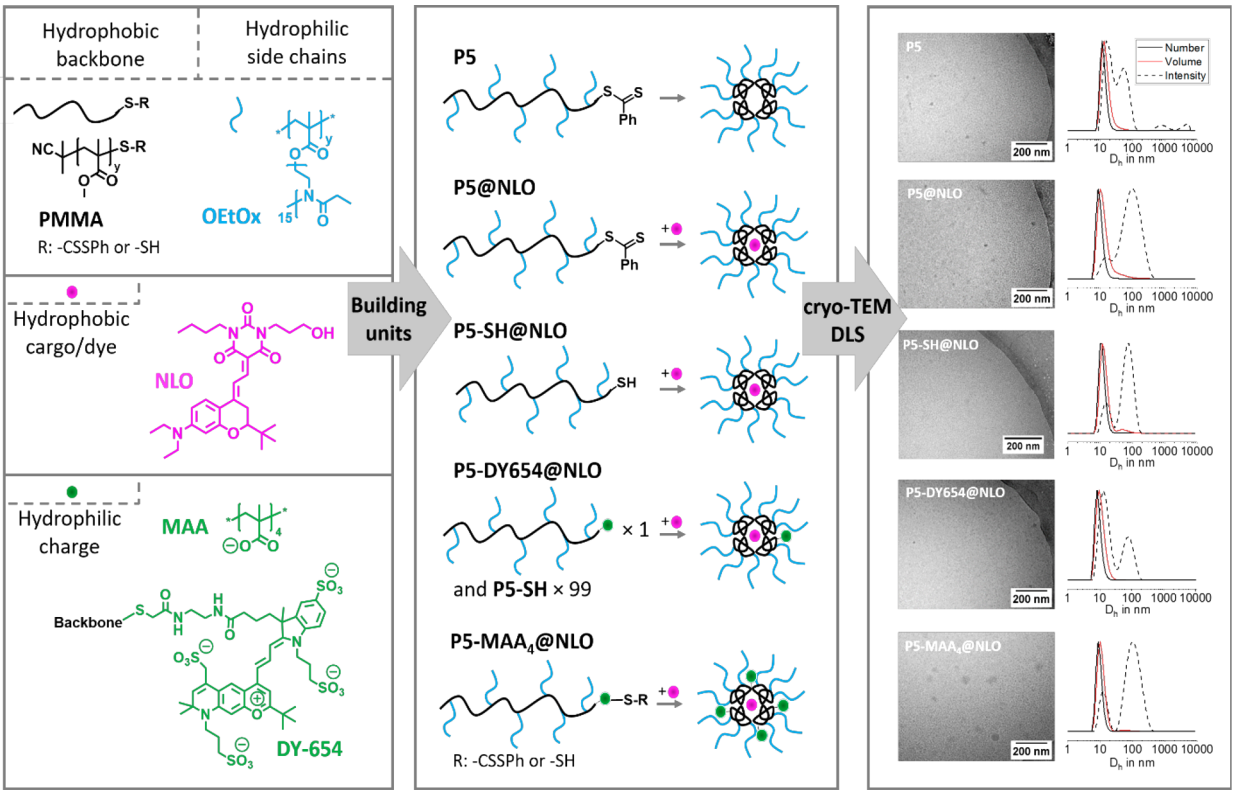

Figure 1. Left: Schematic representation of the building units used to form micelles with different moieties situated between core and shell. PMMA: Poly(methyl methacrylate). $OEtOx_{15}$: Oligo(2-ethyl-2-oxazoline). NLO: Neutral lipid orange. MAA: Methacrylic acid. Middle: Simplified schematic overview of the polymer structures and the proposed micelles formed in aqueous solutions. Right: Aqueous cryo-TEM of micelles of P5 and dye-loaded micelles (concentration of polymer c = 10 mg mL^{-1} in aqueous solution). Dynamic light scattering plots of micelles of P5 and dye-loaded micelles with the number (solid black line), volume (red line), and intensity (dashed line) distributions (concentration of polymer c = 1 mg mL^{-1} in aqueous solution).

Graft copolymers enable a more flexible design than linear block copolymers. In addition to obvious parameters such as the grafting degree and side chain length, additional functional moieties can be introduced[32] at the backbone end groups. Such changes might alter the micellar structures formed and, hence, also influence the stealth effect. Such end group effects are well-known and exploited for micellar carriers composed of end group modified block copolymers. For instance, reduced protein adsorption can be achieved by neutral and slightly negatively charged nanocarriers, while the latter further exhibit lower rates of nonspecific organ uptake.[33,34] However, they have not yet been investigated for graft copolymers, to the best of our knowledge.

Based on these considerations, we synthesized amphiphilic graft copolymers based on poly(methyl methacrylate)-*graft*-oligo(2-ethyl-2-oxazoline) (PMMA-*graft*-OEtOx) and slightly varied their backbone end group to understand their influence on the *in vivo* fate of the loaded nanocarriers. The hydrophilic oligo(2-ethyl-2-oxazoline) (OEtOx)-based macromonomer was copolymerized with the hydrophobic comonomer methyl methacrylate (MMA), thereby ensuring the formation of a comparable hydrophilic OEtOx layer. Subsequently, anionic moieties were introduced at the ω-chain end of the hydrophobic backbone to challenge standard labeling protocols critically. As expected from the known micellization of their PMMA-*graft*-PEG analogues,[35] the polymers self-assembled into core−shell micelles and enabled encapsulation of a hydrophobic dye, which served as a label for the investigation of the uptake and distribution in murine liver cells utilizing intravital fluorescence microscopy.

RESULTS AND DISCUSSION

Oligo(EtOx) was synthesized by cationic ring-opening polymerization (CROP) and end functionalization of the living chain end with triethylammonium methacrylate to result in the macromonomer $EtOx_{15}MA$. Subsequently, the macromonomer method was applied through reversible addition−fragmentation chain transfer (RAFT) copolymerization of MMA and $EtOx_{15}MA$, yielding PMMA-*graft*-$OEtOx_{15}$ graft copolymers comprising a hydrophobic PMMA backbone and hydrophilic OEtOx side chains (Scheme 1). Previously, we identified a graft copolymer composed of 90 mol % of MMA and 10 mol % of $EtOx_{15}MA$ (**P5**) as an optimum for micellar encapsulation of the hydrophobic dye Disperse Orange 3.[37] This statistical copolymer was hence selected as a potential micellar drug carrier to investigate their cell-type specificity in the liver.

P5 was modified by two methods that introduced a small amount of negative charges by modifying their backbone end group. In the first approach, similar to common practice for introducing fluorescent probes, the remaining dithioester end group, resulting from the chain transfer agent (CTA) used during RAFT polymerization was removed quantitatively by aminolysis with hexylamine (Figure SI1). The resulting thiol **P5-SH** was further coupled to the hydrophilic dye DY654 *via* nucleophilic substitution using an iodoacetamide derivative. The successful attachment of the dye **P5-DY654** was validated

https://doi.org/10.1021/acsnano.1c04213
ACS Nano 2021, 15, 12298−12313

Table 1. Key Properties of the PMMA-*graft*-$OEtOx_{15}$-Based Polymers and Micelles

polymer	M_n in g mol^{-1} [a]	$Đ$ [a]	D_h empty micelle [c] (nm)	D_h NLO loaded micelle [c] (nm)	zeta-potential (mV) [d]
P5 [b]	22,900	1.10	number av.: 12	number av.: 11	−27
			volume av.: 18	volume av.: 16	
			intensity av.: 26	intensity av.: 61	
P5-MAA$_4$	22,100	1.15	number av.: 7	number av.: 9	−33
			volume av.: 9	volume av.: 12	
			intensity av.: 20	intensity av.: 50	
P5-DY654	22,700	1.11	number av.: 9	number av.: 11	nd [f]
			volume av.: 11	volume av.: 12	
			intensity av.: 13	intensity av.: 21	
P5-SH	22,700	1.11	number av.: 11	number av.: 11	−20
			volume av.: 13	volume av.: 15	
			intensity av.: 20	intensity av.: 44	
P5 + **P5-MAA$_4$** [e]			number av.: 12	number av.: 10	−20
			volume av.: 16	volume av.: 12	
			intensity av.: 25	intensity av.: 24	

[a]Determined by SEC (DMAc, 0.21 wt % LiCl, RI detection, PMMA calibration). [b]Absolute molar mass determined by analytical ultracentrifugation for **P5** in acetone, *i.e.*, single macromolecule M_n = 24,700 g mol^{-1}, micellar form in water M_n = 231,800 g mol^{-1}, resulting in an aggregation number N_{agg} = 9.4.[34] [c]Determined by dynamic light scattering. Concentration of polymer $c \approx 1$ mg mL^{-1} in aqueous solution at 25 °C, filtered samples with 0.45 μm NY. Loaded micelles contained on average 10 NLO molecules per micelle. [d]Concentration of polymer c = 5 mg mL^{-1} in 0.1 mmol L^{-1} NaCl aqueous solution at 25 °C, filtered samples with 0.45 μm NY. [e]**P5** + **P5-MAA$_4$** represents mixed micelles composed of 1% **P5-MAA$_4$** and 99% of **P5**. [f]Not detectable.

by size exclusion chromatography (SEC) measurements utilizing refractive index and diode array detection (Figure SI2), both revealing a polymer signal at the same elution volume. Also, the absorption and emission spectrum of the dye remained unaffected by the coupling approach, which yielded 99% of polymer chains with thiol end group (*i.e.*, **P5-SH**) and 1% of polymer chains with one dye attached at the backbone end. Attachment of multiple dyes per macromolecule was circumvented by utilizing the end functionalization strategy.

To introduce additional anionic moieties at the same position that would mimic the sulfonate moieties of DY654, the second modification approach relied on the application of **P5** as a macro-CTA in a RAFT polymerization of methacrylic acid (MAA). For this purpose, a short block comprising only four repeating units of MAA was introduced at the end of the graft copolymer backbone, yielding **P5-MAA$_4$**. Consistent with the polymerization mechanism, all polymer chains were modified, while the dithioester end group remained partially present. As targeted, the degree of polymerization (DP) value of the short PMAA block was 4 according to M/CTA× conversion, which was further confirmed by means of acid−base titration of the purified **P5-MAA$_4$** (Figure SI3).

All four **P5**-based polymers spontaneously self-assembled into spherical micelles upon dissolution in water, as determined by means of cryo-transmission electron microscopy (cryo-TEM) and dynamic light scattering (DLS) (Figure 1 and Figures SI4 and SI5). The average **P5** micelles in aqueous solution were formed by 9.4 single polymer chains, as demonstrated previously by analytical ultracentrifugation.[36] The high structural similarity between the polymers suggests similar aggregation numbers for **P5-SH**, **P5-DY654**, and **P5-MAA$_4$**. In accordance with the negative charges introduced at the end of the graft copolymer backbone in **P5-MAA$_4$**, the zeta-potential slightly decreased compared to that of the **P5** and **P5-SH** micelles without anionically charged end groups, although the difference should not be overrated (Table 1). The micelle structure consisting of a hydrophobic PMMA core and a hydrophilic $OEtOx_{15}$ shell allowed the solubilization of the hydrophobic cargo neutral lipid orange (NLO) *via* the thin film method, *i.e.*, the redissolution of a dried polymer−cargo blend in type-1 water followed by purification *via* centrifugation (Figure SI6).[20] Most micelles were able to solubilize at least two NLO molecules per macromolecule (Figures SI7 and SI8). To enable a more straightforward characterization by means of Raman spectroscopy, the NLO content was adjusted to one molecule NLO per polymer chain, *i.e.*, 10 NLO molecules per micelle.

DLS studies suggested the presence of a few larger aggregated structures, which were only observable in the intensity size distribution (Table 1, Figure 1, and Figure SI5). The more representative number distribution indicated hydrodynamic diameters around 10 nm for loaded as well as unloaded micelles. It should, however, be noted that the DLS laser wavelength (λ = 633 nm) limited the characterization of **P5-DY654** micelles due to the absorption range of the DY654.

Cryo-TEM confirmed the presence of spherical micelles with diameters mostly around 10 nm in all samples, regardless if loaded or unloaded (Figure 1 and Figure SI5). The small size is consistent with the micelle composition of only 10 graft copolymer macromolecules and the low DP of the hydrophilic building blocks. Apparently, the small hydrophilicity change of the varied graft copolymer backbone end groups did not affect the micellization in a significant manner.

Raman spectroscopy was performed on the micelles to investigate the effect of these modifications on the structures of otherwise similar micelles.[37] The Raman spectrum of a given molecule captures vibrational frequencies specific to the molecular bonds and the molecule's symmetry. Here, Raman spectroscopy was applied due to its sensitivity to conformational changes. The molecular arrangement of the polymer leading to conformational changes exhibits vibrational signatures in the Raman spectrum. Thus, conformational changes in the micelles will alter the resulting molecular fingerprint, and the Raman peak positions allow one to pinpoint the contributing molecular vibrations. For the analysis, the micelle solutions were preconcentrated by

https://doi.org/10.1021/acsnano.1c04213
ACS Nano 2021, 15, 12298−12313

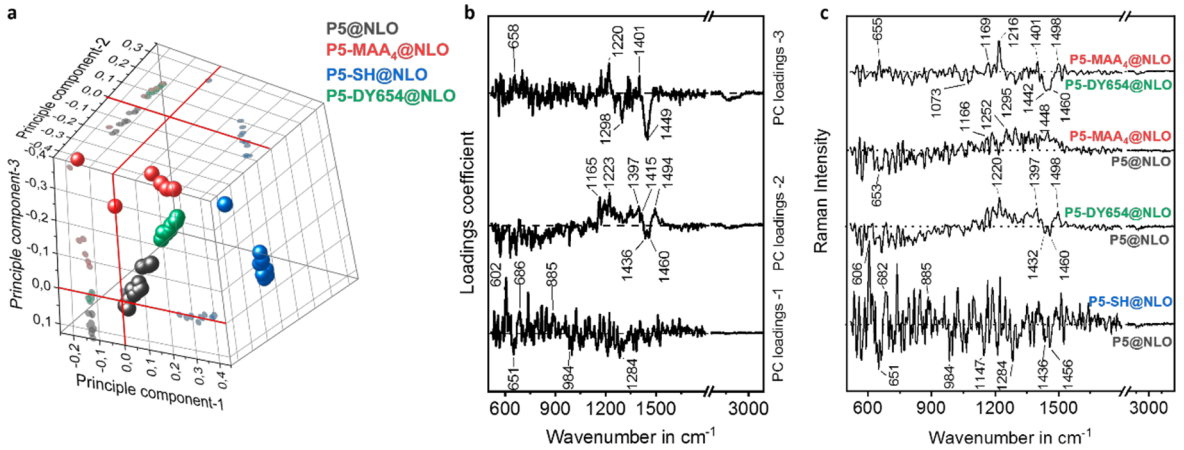

Figure 2. Hydrophilicity induces changes in the micellar confirmation. Raman spectra from micelles were obtained in liquid-state. (a) Principal component analysis of the Raman spectra of P5@NLO and the more hydrophilic micelles P5-DY654@NLO, P5-MAA$_4$@NLO, and P5-SH@NLO. The spectral differences in the micelles can be visualized in the 3D-PC score plot obtained using PC-1, PC-2, and PC-3. 2D PC score plots are provided in Figure SI9. (b) Loading coefficients PC-1, PC-2, and PC-3 and (c) difference Raman spectra display the relative Raman spectral changes between the micelles.

evaporation due to exposure to the laser while recording Raman spectra. After the measurements, the micelle solutions were visually inspected under the microscope and exhibited no change in their physical state.

Furthermore, to understand the spectral differences observed in the Raman spectra of the micelles and trace vibrations to their molecular origin, Raman spectra of the pure substances, *i.e.*, the dyes NLO and DY654, **P5**, PMAA, PMMA, and PEtOx were also recorded (Figure SI9). The Raman fingerprints of micelles loaded with NLO (**P5@NLO**, **P5-DY654@NLO**, **P5-MAA$_4$@NLO**, and **P5-SH@NLO**) in solution were compared with the reference substances, revealing that the micelles' Raman spectra are dominated by strong NLO signals accompanied by a high spectral noise due to strong fluorescence background from the NLO. To investigate the fine differences present in the Raman spectra of the micelles, principal component analysis (PCA) was performed. PCA is an unsupervised analysis method, which does not require manual classifications. PCA utilizes the Raman spectral features such as Raman band position, intensity, band shape, or noise to cluster Raman spectra according to similarity. Furthermore, the PCA loadings provide information about the contributing Raman peaks, allowing one to visualize the separation of respective groups in the PCA score plot (Figure 2a and Figure SI10). These spectral differences can be visualized from the PC loading coefficients shown in Figure 2b. The performed PCA led to a clear differentiation of **P5-MAA$_4$@NLO** from **P5@NLO** and **P5-DY654@NLO** by the principal component PC-3. The Raman peaks at 658, 1220, and 1401 cm^{-1} belong to **P5-MAA$_4$@NLO** with positive PC-3 scores. The Raman peaks at 1298 and 1449 cm^{-1} belong to **P5-DY654@NLO** and **P5@NLO** with negative PC-3 scores. PC-2 distinguished **P5@NLO** (1436 and 1460 cm^{-1}) from the other micelles, whereas PC-1 separated **P5-SH@NLO**. The negative Raman peak visible in the PC-1 at 651 cm^{-1} belongs to NLO in all micelles except **P5-SH@NLO**. The positive peaks at 602 and 686 cm^{-1} correspond to **P5-SH@NLO**.

The changes in the micelles captured by the loadings were also observed in the difference Raman spectra displayed in Figure 2c. As can be seen from the 3D score plot, all four micelles formed distinct clusters and were well-separated from each other. Hence, Raman spectroscopy provided experimental evidence of different molecular arrangements within the micelles due to the different end groups, altering the environment of the NLO dye within the carriers.

Before the fate of the micellar assemblies were tested in *in vitro* and *in vivo* experiments, their integrity was in focus, as dilution and the presence of biological media might affect their structure. The blood volume of mice is generally calculated with 58.5 mL of blood/kg body weight. Considering the amounts injected *in vivo* in this study (150 μg per animal), an initial blood concentration of 103 μg mL^{-1} is expected in a 25 g mouse (average body weight of mice used in the study). Analytical ultracentrifugation measurements of diluted samples were hence performed at such concentrations and even below (40 μg mL^{-1}). Results confirmed the integrity of the loaded micelles in water with assemblies containing cargo even at the lowest concentration investigated and with hydrodynamic sizes consistent to DLS and cryo-TEM (see Supporting Information for details, Figure SI11). In addition, DLS indicated the stability of the loaded micelles in physiologically relevant buffers (KHB and PBS) at 37 °C (see Supporting Information, Figure SI12). In fact, loaded micelles were directly formed in these buffers *via* the thin film method. These findings are supported by free-flow electrophoresis (FFE) performed in the presence of albumin, the most abundant plasma protein, indicating the stability of the micelles and successful shielding of the NLO cargo from interaction with albumin (see Supporting Information, Figure SI13).

Primary mouse embryonic fibroblasts (MEFs) are a valuable source for primary cells to study the uptake route of the various micelles in model cells. MEFs do not exhibit classical tumor mutations that are known to impact endocytosis and pinocytosis rates.[38] Their embryonic origin results in delayed senescence and stable metabolic activity while also exhibiting fully functional endocytic and pinocytotic pathways over multiple passages.[39] In *in vitro* studies, none of the micelles showed toxicity after 24 h in MEFs (Figure SI14). A rapid cellular uptake (after 10 min) and similar intracellular distribution of the cargo NLO (in DMSO) and the NLO-loaded micelles were observed *in vitro*. Incubating cells with

https://doi.org/10.1021/acsnano.1c04213
ACS Nano 2021, 15, 12298−12313

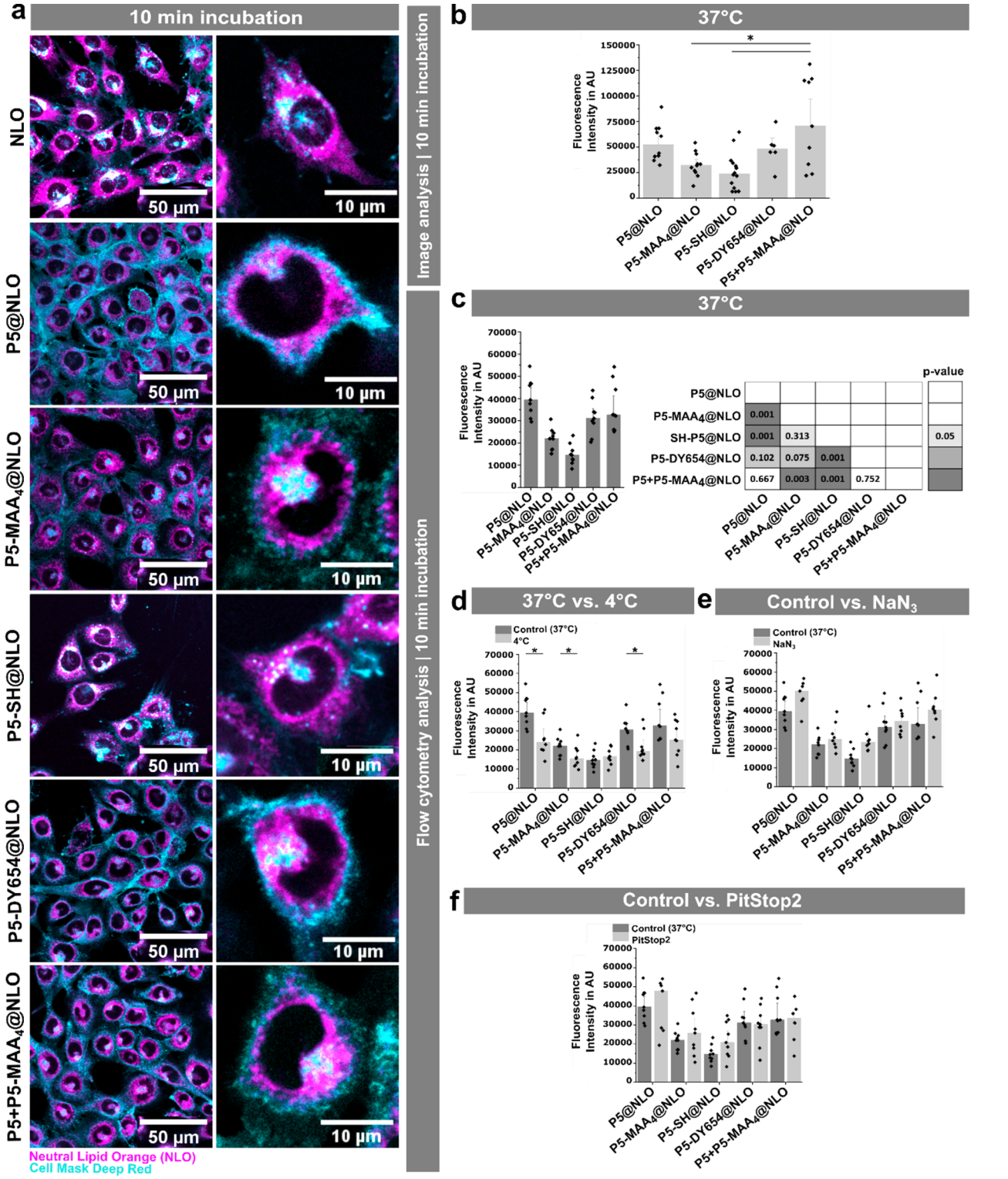

Figure 3. Influence of end group modifications of graft copolymer micelles on endocytosis-independent uptake *in vitro*. (a) Live cell imaging of cell masks deep red (cyan)-stained MEFs, incubated 10 min with 20 nmol L^{-1} NLO (magenta) or 50 μg mL^{-1} NLO-loaded micelle. (b) Quantification of fluorescence intensities from fluorescent images. One-way ANOVA between groups, $*p < 0.05$. (c) Flow cytometry analysis of MEFs, incubated 10 min with 50 μg mL^{-1} NLO-loaded micelles. Heatmap of p values from a parametric one-way ANOVA between groups with a Tukey posthoc test for pairwise differences, $n = 3$. (d–f) Uptake of various micelles in the presence of different inhibitors determined by flow cytometry, unpaired t test control *vs* treatment, $*p < 0.05$. (d) Uptake of various micelles at 4 or 37 °C. (e) Uptake of various micelles in the presence of 10 mmol L^{-1} NaN_3. (f) Uptake of various micelles in the presence of 30 μmol L^{-1} Pitstop-2. By unpaired t test control *vs* treatment, $*p < 0.05$, no statistical difference between control and treatment for (e) and (f) was found. (b–f) Intensities were corrected for intrinsic intensity and NLO loading differences. Data are shown as median + standard deviation, and individual values are depicted as dots.

https://doi.org/10.1021/acsnano.1c04213
ACS Nano 2021, 15, 12298–12313

Table 2. Qualitative Assessment of the *In Vivo* Uptake in Different Cell Types[a]

micelle	anionic charge	DTB (hydrophobic)	Kupffer cells	hepatocytes	LSEC	calculated $t_{1/2}$
P5-SH@NLO	none	none	+	+	nd[b]	++++
P5-DY654@NLO	+	none	++	++++	nd[b]	+++
P5-MAA$_4$@NLO	++++	+	+++	++	+	+++++
P5@NLO	none	+++	++++	+++	nd[b]	+
P5 + P5-MAA$_4$@NLO	+	+++	+++++	+++++	++	++

[a]Data were sorted according to uptake in Kupffer cells. The signal intensity for the observation was compared for the micelles (from + (lowest) to +++++ (highest) signal) [b]Not detected.

NLO led to staining of perinuclear, elongated organelles, *e.g.*, mitochondria or endoplasmic reticulum. NLO-loaded micelles preferentially accumulated in similarly shaped perinuclear compartments (Figure 3a). NLO fluorescence intensity in cells was highest when incubated with the micelles composed of graft copolymers featuring hydrophobic dithiobenzoate end groups, **P5@NLO**. The negative charges introduced at the interface of the micellar core and shell achieved by the terminal modification of **P5** with four units of methacrylic acid or DY654 (which possess four sulfonic residues) gradually decreased the uptake efficiency, indicating an improved shielding of these micelles (Figure 3b). Since chain extension of **P5** with MAA was quantitative but labeling with DY654 was only 1% while remaining polymer chains were left with a terminal −SH group, the question occurred whether the differences can be attributed to charge or hydrophilicity. To mimic the **P5-DY654** micelle, **P5**, comprising a hydrophobic end group, was combined with the MAA-modified **P5-MAA$_4$** to yield a mixture where 1% of the molecules carried the terminal charge. The resulting NLO-loaded micelle (**P5 + P5-MAA$_4$@NLO**) accumulated in MEFs as efficiently as **P5@NLO**, highlighting the importance of the presence or absence of the dithiobenzoate end group for the performance of these micelles. As 99% of **P5-DY654** comprised graft copolymers with a terminal thiol moiety, micelles exclusively formed from **P5-SH** were compared. **P5-SH@NLO** revealed the lowest cellular uptake under serum-free incubation conditions in this study using microscopy and flow cytometry analysis (Figure 3b,c). That hints toward a more pronounced effect of the hydrophobicity of the end group (**P5** *vs* **P5-SH**) compared to that of negative charges (**P5** *vs* **P5-MAA$_4$**).

Performing the experiments at 4 °C decreased the uptake of **P5@NLO**, **P5-MAA$_4$@NLO**, and **P5-DY654@NLO** in MEFs significantly in comparison to the control experiments performed at 37 °C (Figure 3d). Protein absorption can be a confounder of uptake processes and impact the uptake route. The uptake rates at 37 and 4 °C were similar when those experiments were performed in the presence of 10% fetal bovine serum to the medium for the micelles investigated here (Figure SI14c), thereby indicating the independence of the uptake from the interaction with serum proteins *in vitro*. Further experiments were carried out to exclude the endocytic uptake of those micelles under serum-free conditions. Before the incubation with micelles, we treated cells with the ATPase inhibitor sodium azide, which inhibits various active uptake mechanisms in cells but did not affect the uptake of the micelles (Figure 3e). Pitstop-2, a known inhibitor for preferentially clathrin-mediated endocytosis,[40,41] did not reduce micellar uptake (Figure 3f). We further validated these findings using MEFs expressing a marker for clathrin-mediated endocytosis, early endosome antigen (EEA) 1, fused to the green fluorescent protein (GFP). Analyzing EEA1-GFP-positive vesicles in the perinuclear and peripheral regions of the cells, we did not find any specific NLO accumulation in these vesicles (Figure SI16). These results indicate that the uptake of micelles is independent of the cellular energy level and does not require clathrin-mediated endocytosis. The filamentous perinuclear staining pattern was visible as early as 10 min after adding the micelles. Together with the temperature sensitivity of the uptake, our data suggest a direct translocation through the cell membrane, *e.g.*, by penetration, without a rate limitation by active, energy-dependent endocytosis.[42]

The effects seen in the cell culture translate to the *in vivo* situation. Intravital microscopy (IVM) of the liver was applied to study pharmacokinetics. The liver is a significant clearance organ and allows the assessment of the nanocarrier interaction with parenchymal cells (hepatocytes) and a majority of cell types commonly summarized as the reticuloendothelial system. Cells of the RES are specialized to recognize different foreign bodies and thus also nanocarriers.[43] In the liver, circulating immune cells (lymphocytes),[37,44,45] Kupffer cells (livers' local macrophages),[46−50] liver sinusoidal endothelial cells (LSECs, livers' specialized endothelial cells),[46−50] and hepatocytes come together, forming a powerful barrier able to clear a large variety of nanocarriers.[37,44,45,51] After cells of the RES engulf nanocarriers, they signal to their environment, which in many cases triggers an immune response, potentially causing hypersensitivity or, in rare cases, even anaphylactic reactions.[13,52] Their distinct morphology and tissue distribution allow their (automated) identification without additional staining once they take up the fluorescent cargo and appear in the images. Circulating immune cells are recognized by IVM due to their specific location in the sinusoids and their mobility, *i.e.*, their movement in time-lapse microscopy. Lymphocytes become only visible in fluorescence IVM through staining by the used payload NLO. No NLO-positive circulating cells were observed in the capillaries (Video S6). These results suggest that the uptake by circulating immune cells has little impact on the clearance of the investigated micelles. The clearance of the different micelles by hepatocytes, LSECs, and Kupffer cells varied (Table 2). Their strong NADPH autofluorescence enables one to identify hepatocytes without further staining. The discrimination of LSECs and Kupffer cells was confirmed by antibody-based *in vivo* F4/80 staining at the end of each experiment to circumvent interference with carrier-cell interaction (Figure 4a,b). Their unique location along the sinusoids discriminates LSECs at the interphase between NADPH-negative and -positive structures (Figure 4b). Hepatocytes are parenchymal cells located behind the fenestrated capillaries formed by LSECs. Kupffer cells are located in those capillaries, exposing large surfaces into the capillary lumen and interacting with molecules passing by. The amount of the micelles passing

https://doi.org/10.1021/acsnano.1c04213
ACS Nano 2021, 15, 12298−12313

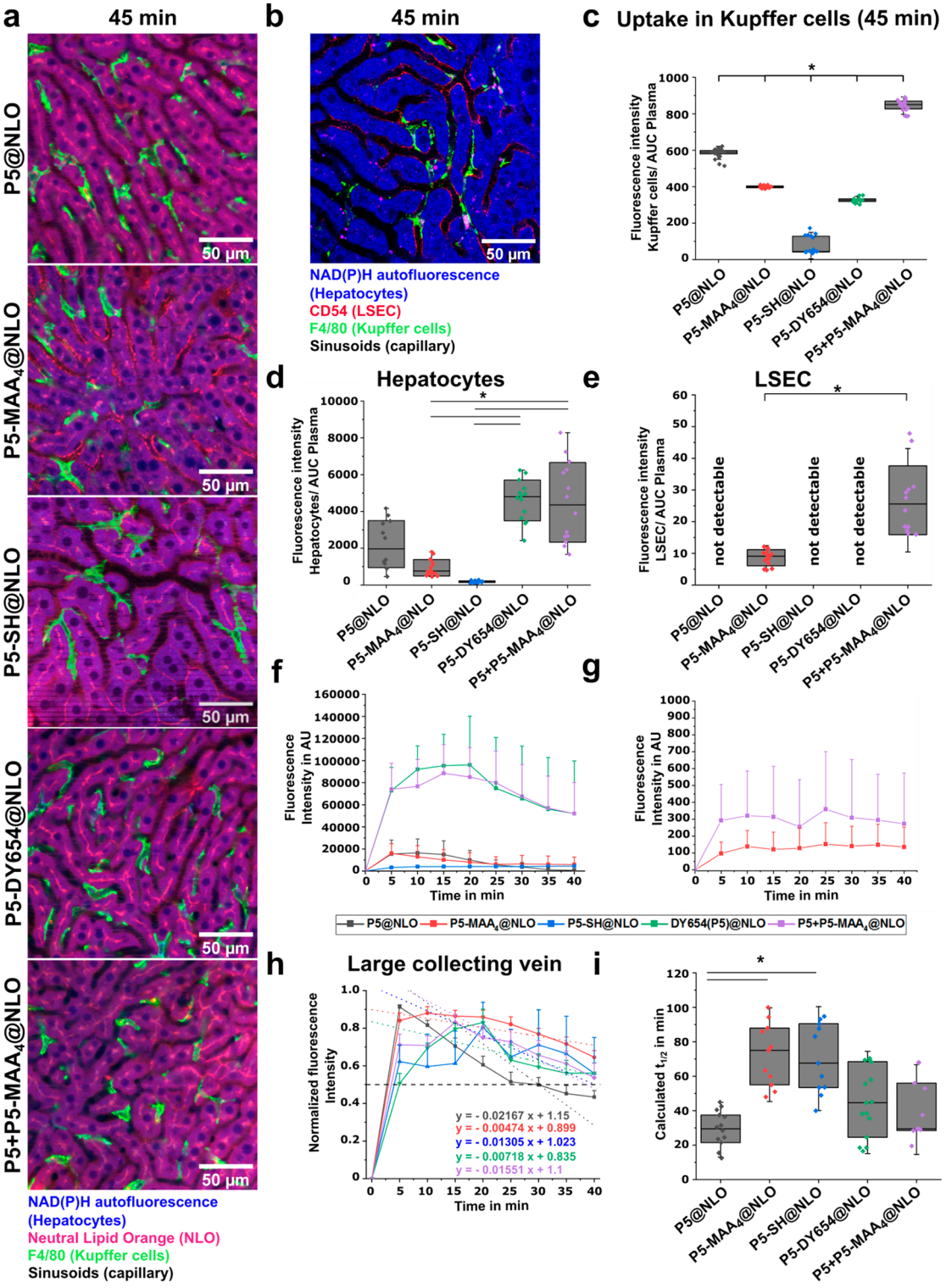

Figure 4. End group modifications of graft copolymer micelles influence cell-type-specific uptake in the liver and mediates stealth effects. (a) Intravital microscopy of murine liver 45 min after injection of NLO-loaded micelles. Their NADPH autofluorescence visualizes hepatocytes. Kupffer cells were counterstained with an F4/80-FITC (green) antibody, injected at the end of the experiment. (b) (Co)localization of sinusoids (black) and liver cells commonly contributing to nanocarrier clearance: Hepatocytes are identified by their high NADPH autofluorescence (blue). LSECs stained with anti-CD54 APC (red) and Kupffer cells with anti-F4/80 FITC (green). (c–e) All data were normalized by the AUC to account for differences in the absolute accumulation of the various micelles in the liver. (c) Mean NLO fluorescence intensity in Kupffer cells. (d,e) Maximal NLO fluorescence intensity in hepatocytes and LSECs. (f,g) Uptake and elimination kinetics of NLO by hepatocytes and LSECS. (h) Normalized fluorescence intensity of circulatory half-life quantified from intravital microscopy time series of large portal vein branches in the liver. (i) Calculated circulatory half-life ($t_{1/2}$). (c,d,e,i) Data are depicted as median (line), box plots indicate 25, 75 percentile, whiskers reflect standard deviation, one-way ANOVA between groups, Tukey test, *p < 0.05. Five areas (425 μm^2 each) of each liver were analyzed from 3 to 4 mice per group.

https://doi.org/10.1021/acsnano.1c04213
ACS Nano 2021, 15, 12298–12313

through the liver during the imaging period may bias the amount that is taken up by the different cell types. To obtain comparable data on the uptake of the individual micelles in the different liver cells, we analyzed the plasma disappearance from large veins in the liver and calculated the area under the curve (AUC) (Figure SI20). This enabled us to estimate the amount of NLO that passed through the liver and normalize to the accumulation of NLO signals in the different cells. **P5@NLO** composed of graft copolymers with the hydrophobic dithiobenzoate end group was cleared by hepatocytes (Figure 4d,f), accumulated rapidly in Kupffer cells (Figure 4c), but was not detected in LSECs (Figure 4e,g). It also had the lowest plasma half-life among the various micelles studied (Figure 4i), indicating an overall rapid uptake and clearance by the liver. The micelle without dithiobenzoate moieties and charges (**P5-SH@NLO**) differed substantially from **P5@NLO**. **P5-SH@NLO** micelles were characterized by one of the most extended circulation times of all micelles investigated (Figure 4i) and were poorly taken up by hepatocytes and Kupffer cells (Figure 4d,c). Similar to **P5@NLO**, they did not accumulate in LSEC (Figure 4e). The addition of a charged end group in **P5-MAA$_4$@NLO** only slightly reduced the uptake in Kupffer cells and hepatocytes compared to **P5@NLO** (Figure 4c,d) but led to recognition and uptake by LSEC (Figure 4g,e). While the cell-type-specific clearance pattern in the liver was altered, the overall half-life increased to the level of **P5-SH@NLO** (Figure 4i), indicating that the end group modification affects the uptake in other tissues as well. Reducing the density of MAA$_4$-labeled chains to 1% in **P5 + P5-MAA$_4$@NLO** increased the uptake of the micelles in hepatocytes, Kupffer cells, and LSEC to a level above that of **P5@NLO** (Figure 4c–e). The substantial clearance in the liver might result from a better cell interaction of the micelles with surfaces and surface receptors,[53,54] likely due to rearrangement of the micellar shell exposing anionic methacrylate moieties on the micelles. The labeling of the graft copolymers by DY654 increased accumulation in hepatocytes (Figure 4d) and to a lesser extent in Kupffer cells (Figure 4c) but did not result in uptake by LSECs (Figure 4e).

Overall, the micelles without or with only a small amount of hydrophobic dithiobenzoate showed increased stealth properties, *i.e.*, reduced uptake in Kupffer cells and increased plasma half-life time (Table 2). However, the exemption was the mixed micelle **P5 + P5-MAA$_4$@NLO** that stimulated the uptake by Kupffer cells (Figure 4c) and minimally increased the circulation time (Figure 4i). The use of charged terminal groups (MAA$_4$, DY654) resulted in increased recognition by hepatocytes compared to the uncharged, more hydrophilic micelle **P5-SH**, possibly due to recognition as anionic moieties that can interact with anionic transporters on the hepatocyte surface.[55] In contrast to the similarly charged DY654, the MAA$_4$ moiety resulted in recognition and uptake by LSECs in the liver. Previous studies have already observed a methacrylic acid content-dependent recognition of polymethacrylate-based nanoparticles by LSECs in the liver,[56] giving rise to the question of whether methacrylic acid-based anionic charges may serve as a basis of targeting moieties in nanocarriers. These effects occurred even though the charges were located at the interface of the micellar core and shell, *i.e.*, without being directly exposed as end groups of the OEtOx building blocks forming the shell.

These different uptake kinetics and cellular distributions in the liver might be a consequence of direct and indirect effects, such as differences in the interaction with cell surface factors such as sugars or, *e.g.*, organic anion receptors, or changes in the quality and quantity of adsorbed proteins.[57,58]

CONCLUSION

Micelles formed from graft copolymers comprising the PEG alternative OEtOx have a high potential as polymeric drug carriers. An efficient stealth effect introduced by a dense layer of multiple short OEtOx chains around a hydrophobic PMMA core was evident from a strongly reduced uptake of very small micelles in Kupffer cells. Despite the high molar mass of the graft copolymers of 20 kg mol^{-1}, the hydrophobic backbone end group strongly affected the micelles' liver clearance and stealth effect. The hydrophobic dithiobenzoate end group resulted in a considerable increase in uptake of the micelles by Kupffer cells, *i.e.*, loss of stealth properties, an effect that was avoided by cleavage of the end group or introduction of a few anionic charges per macromolecule.

It was hence evident that minimal alterations of the macromolecule, similar or equal to those made by labeling with fluorescent probes, strongly altered the micelles' stealth properties and liver clearance. The direct and tailored end group modification approach presented here enabled us to unravel hydrophobicity and charge effects systematically. This implies that the design of macromolecular carriers remains a delicate matter. Aside from obvious parameters, such as block ratio and chain length of linear amphiphilic polymers, significant effects can arise from minor end group modifications introduced at the interface between core and shell of the micelles composed of amphiphilic graft copolymers.

METHODS

Materials Used for the Synthesis. All chemicals and solvents were obtained from standard commercial sources and used without further purification unless otherwise stated. 2-Ethyl-2-oxazoline (EtOx) was dried over barium oxide and distilled under argon atmosphere before use. Methyl *p*-toluenesulfonate (MeTos) was distilled and stored under argon. 2,2′-Azobis(2-methylpropionitrile) (AIBN, 98%) was purchased from Acros and recrystallized from methanol. The CTA 2-cyanopropyl dithiobenzoate (CPDB, 97%) was obtained from Strem Chemicals. Methyl methacrylate and methacrylic acid were flushed through a short column filled with an inhibitor remover prior to use. Dyomics GmbH kindly provided DY654-iodoacetamide and neutral lipid orange (NLO). The albumin protein was purchased from SERVA (bovine albumin fraction V, protease and fatty acid-free, diagnostic grade lyophilic, M_r = 67,000.00 g mol^{-1}). The Krebs–Henseleit buffer (modified with 2 g L^{-1} glucose) and phosphate-buffered saline (pH 7.4) were purchased from Sigma-Aldrich. PMMA and PMAA used as reference materials for Raman spectroscopy were synthesized by RAFT polymerization as previously described.[59]

Synthesis. *EtOx$_{15}$MA.* The oligo(2-ethyl-2-oxazoline) methacrylate (EtOx$_{15}$MA) was synthesized as previously published.[36] Briefly, 0.74 g (4 mmol) of MeTos, 5.95 g (60 mmol) of EtOx, and 8.97 mL of acetonitrile were transferred into a preheated vial under inert conditions. The polymerization was performed in the microwave synthesizer (Biotage Initiator+) at 140 °C for 60 s. Subsequently, 0.52 g (6 mmol) of methacrylic acid (MAA) and 0.81 g (8 mmol) of triethylamine (NEt$_3$) were added, and the reaction solution was kept at 50 °C overnight. The reaction mixture was dissolved in chloroform, washed with aqueous sodium bicarbonate solution and brine, dried over sodium sulfate, and concentrated under reduced pressure. DP = 15.5, DF = 0.90.

P5. The PMMA-*graft*-OEtOx$_{15}$ was synthesized as previously published.[35] Briefly, 1.0 g (0.6 mmol) of EtOx$_{15}$MA, 252.4 mg (2.5 mmol) of MMA, 1.4 mg (8.8 μmol) of AIBN, and 7.7 mg (35 μmol)

https://doi.org/10.1021/acsnano.1c04213
ACS Nano 2021, 15, 12298–12313

of CPDB were dissolved in ethanol at an overall monomer concentration $[M]_0$ of 1 mol L^{-1} ([M]/[CPDB]/[AIBN] ratio of 90:1:0.25). The reaction solution was gently degassed by argon bubbling and subsequently heated at 70 °C overnight. The raw product was purified by preparative SEC (BioBeads SX-1 from Bio-Rad in THF) and characterized by means of SEC and ^{1}H NMR spectroscopy. Conversion: 88%. Composition: 89 mol % of MMA. SEC (LiCl in DMAc, RI detection, PMMA calibration): M_n = 22,900 g mol^{-1}, $Đ$ = 1.10.

P5-SH. First, 0.3 g (14 μmol) of **P5** and 0.1 g (0.9 mmol) of hexylamine were dissolved in CH_2Cl_2 (2 mL each), degassed by argon bubbling, subsequently combined, and stirred overnight at room temperature. The raw product was purified by precipitation in cold diethyl ether. SEC (LiCl in DMAc, RI detection, PMMA calibration): M_n = 22,700 g mol^{-1}, $Đ$ = 1.11. SEC (LiCl in DMAc, DA detection at 311 nm, PMMA calibration): no polymer signal.

P5-DY654. For this compound, 0.17 g (8.2 μmol) of **P5-SH** and 1 mg (0.82 μmol) of DY654-iodoacetamide were dissolved in 4 mL of DMF, degassed by argon bubbling, and stirred in the dark at room temperature for 72 h. The raw product was purified by column chromatography (Sephadex G-25 Medium from Sigma-Aldrich in water). The successful coupling of the dye and the polymer purity were verified by SEC measurements with simultaneous RI and DA detection at 656−658 nm. Labeling efficiency of 8% was determined by UV−VIS absorption spectroscopy (Analytik Jena SPECORD 250) using a calibration curve generated from a serial dilution of the dye at the absorption maximum in water (λ = 566 nm). SEC (LiCl in DMAc, RI and DA detection, PMMA calibration): M_n = 22,700 g mol^{-1}, $Đ$ = 1.11.

P5-MAA$_4$. First, 0.2 g (9.1 μmol) of **P5**, 0.37 mg (2.3 μmol) of AIBN, and 7.9 mg (91.3 μmol) of MAA were dissolved in ethanol, degassed by argon bubbling, and heated at 70 °C for 72 h. To determine the MAA conversion (40%, corresponding to a DP value of 4), aliquots were taken before and after heating and analyzed by means of ^{1}H NMR spectroscopy. The reaction mixture was dissolved in $CHCl_3$ (50 mL), washed with water (3 × 50 mL), dried over sodium sulfate, concentrated, and dried under reduced pressure at 40 °C. The DP of 4 for the MAA block was additionally determined by acid/base titration. For this purpose, the polymer was dissolved in deionized water, and 1 mL of 0.1 M hydrochloric acid solution was added. The titration was performed against 0.1 M aqueous sodium hydroxide solution using a 765 Dosimat from Metrohm, a digital pH/mV thermometer GMH 3530 from Greisinger Electronic, and the EBS 20M Recorder software. SEC (LiCl in DMAc, RI detection, PMMA calibration): M_n = 22,100 g mol^{-1}, $Đ$ = 1.15.

NMR Spectroscopy. Proton nuclear magnetic resonance (^{1}H NMR) spectra were recorded at room temperature in $CDCl_3$ on a Bruker Avance 300 MHz using the residual solvent resonance as an internal standard. The chemical shifts are given in parts per million.

Size Exclusion Chromatography. A Shimadzu system with a PSS degasser, a G1362A RI detector, a G1315D DA detector, a G1310A pump, a G1329A autosampler, a Techlab oven, and a PSS GRAM guard/30/1000 Å column with a 5 μm particle size was used. The system was run with an eluent composed of *N*,*N*-dimethylacetamide with 0.21% LiCl at a flow rate of 1 mL min^{-1} at 40 °C and was calibrated with PMMA standards (~400 to 1,000,000 g mol^{-1}).

Neutral Lipid Orange Encapsulation. The encapsulation experiments were performed according to a procedure established previously for Disperse Orange 3.[36] Polymer and dye solutions in acetone were prepared to yield molar ratios of [P] to [NLO] of 1:1, 1:2, 1:3, 1:4, and 1:5. Subsequently, the solvent was removed to complete dryness. Water was added, and the mixture was stirred overnight. The non-encapsulated dye was removed by centrifugation (ROTINA 380 R from Andreas Hettich GmbH & Co. KG D-78532 Tuttlingen equipped with a fixed-angle rotor), and supernatant was freeze-dried (Alpha 2-4 LDplus from Martin Christ Gefriertrocknungsanlagen GmbH). The solid material obtained was dissolved in acetone, and the dye uptake was determined by means of UV−vis absorption spectroscopy at room temperature (Analytik Jena SPECORD 250 spectrometer) using a calibration curve generated from a serial dilution of the dye at the absorption maximum in acetone (λ = 556 nm).

For the formulation of **P5@NLO** in PBS and KHB, the respective buffers were simply added to the thoroughly dried thin film (here, the same ratio of **P5** to NLO was used as for the animal experiments), purified by centrifugation, and measured by DLS at 37 °C.

Dynamic Light Scattering and Zeta-Potential. For unloaded micelle solutions, the respective polymer was directly dissolved in Milli-Q water. For the NLO-loaded micelles, the supernatant after centrifugation was used. DLS measurements were performed using a Zetasizer Nano ZS (Malvern Instruments, Herrenberg, Germany). After an equilibration time of 180 s, 3 × 30 runs were carried out at 25 °C (λ = 633 nm). The counts were detected at an angle of 173°, and mean particle size was approximated as the effective (*Z*-average) diameter obtained by the cumulants method assuming a spherical shape. Each measurement was performed in triplicate.

DLS measurements of **P5-DY654** and **P5-DY654@NLO** as well as zeta-potential measurements of unloaded micelles were performed using a Zetasizer Ultra (Malvern Instruments, Herrenberg, Germany). The detection angles were fixed by the manufacturer at an angle of 173° for DLS and at an angle of 17° for zeta-potential. For DLS measurements of DY654-containing samples, an optical fluorescence filter was used. After an equilibration time of 30 s, three measurements with up to 30 runs were carried out at 25 °C (λ = 633 nm). Zetasizer Nano Series disposable folded capillary cells (DTS1070, Malvern) were used for zeta-potential measurement, and low volume disposable cuvettes (ZEN0040, Malvern) were used for DLS. The mean particle size was approximated as the effective (*Z*-average) diameter obtained by the cumulants method assuming a spherical shape. Sample preparation for zeta-potential measurements of unloaded micelles included the direct dissolution of the respective polymer in 0.1 mmol L^{-1} aqueous NaCl and subsequent filtration with a prewetted 0.45 μm Nylon 66 13 mm syringe filter. The data were evaluated with the ZS XPLORER 1.5.0.163 software.

Cryo-Transmission Electron Microscopy. The sample preparation was performed as described above (DLS section). Cryo-TEM investigations were conducted on an FEI Tecnai G^2 20 with an acceleration voltage of 200 kV. Samples (8.5 μL) were applied onto Quantifoil grids (Quantifoil, Germany, R2/2) utilizing a Vitrobot Mark IV vitrification system and were transferred to the cryo-TEM holder (Gatan, USA) utilizing a cryo stage. Images were acquired on a 1 × 1 k or a 4 × 4 k CCD camera.

Raman Spectroscopy. The Raman spectra of polymer micelles were recorded using an upright micro-Raman spectrometer (CRM 300, WITec GmbH, Germany) benchtop system equipped with 785 nm laser (laser power 70 mW at the sample plane), a 300 g mm^{-1} grating, and a deep depletion CCD camera. The liquid suspension of the samples of ~5 μL was placed on the CaF_2 slide, and 10 single spectra were acquired using a 100× objective (NA 0.75, Zeiss) at different positions with 1 s laser exposure time per spectrum. The reference substances (PMMA, $EtOx_{15}MA$, PMAA) were recorded using an upright micro-Raman spectrometer (InVia-Qontor Renishaw, UK) benchtop system equipped with a 785 nm laser (laser power 23 mW at the sample plane), a 1200 g/mm grating, and a CCD camera. The liquid suspension of the samples of ~5 μL was placed on the CaF_2 slide, and 10 single spectra were acquired using a 50× objective (NA 0.75, Leica) at different positions with 10 s exposure time per spectrum. During Raman spectral recording, white light images were acquired to control the liquid state of the polymer samples. The Raman spectra of NLO and DY654 were recorded in the solid state using a hand-held Raman spectrometer (Progeny, Rigaku Analytical Devices, USA) equipped with a 1064 nm laser (laser power 100 mW at the sample plane). Raman spectra of the powder dye sample were collected from three different positions. Each spectrum was collected with 0.5 s laser exposure time per spectrum. The Raman spectra of the dyes were collected with 1064 nm because, with the 785 nm excitation wavelength, both NLO and DY654 displayed a high fluorescence background. The raw Raman spectra acquired using the benchtop system were preprocessed in GNU R

https://doi.org/10.1021/acsnano.1c04213
ACS Nano 2021, 15, 12298−12313

using in-house built algorithms. The Raman spectra containing cosmic spike and artifact, *e.g.*, high noise, were removed before analysis. The Raman spectra were background corrected by applying the SNIP algorithm (1) and vector normalized. An average spectrum along with a standard deviation was generated for the display. Principal component analysis was performed using preprocessed Raman spectra of **P5@NLO**, **P5-DY654@NLO**, and **P5-MAA$_4$@NLO**. The analysis was done on GNU R platform. PCA scores and loadings coefficients were generated. For displaying Raman spectroscopy data, OriginPro 2016 (Sr2 b9.3.2.303, OriginLab Corporation) was used.

Analytical Ultracentrifugation. Multidetection sedimentation velocity experiments were performed as described recently.[36] They were conducted using an Optima Analytical Ultracentrifuge (Beckmann Coulter Instruments, Brea, CA) with an An-50 Ti eight-hole rotor spun at 42,000 rpm at a temperature of 20 °C. The cells contained double sector Epon centerpieces with a 12 mm solution optical path length and sapphire windows. Those were filled with approximately 440 μL water as a reference and approximately 420 μL of sample solutions diluted in water. Scans were acquired in 3 min intervals using the interference optics and absorbance optical detection system. The radially resolved interference fringes and optical density at a wavelength of 550 nm that is representative of NLO were recorded. The recorded sedimentation velocity data were numerically analyzed with SEDFIT and the ls−g*(s) model considering nondiffusing species.[60] For molar mass and hydrodynamic diameter estimations, established routines were used.[61,62]

Free-Flow Electrophoresis. Free-flow electrophoresis (FFE) was measured on a system kindly made available to us by FFE Service GmbH (Feldkirchen, Germany). The device was equipped with a separating chamber front piece of 500 × 100 × 0.2 mm and a chamber volume of 10.9 mL, an S5 inlet, a cooler with the temperature set to 10 °C, a tube diameter of 0.51 mm, a PP60 membrane, a spacer with a thickness of 0.2 mm and paper filter of 0.3 mm. The anode and the cathode solution contained 150 mmol L^{-1} isobutyric acid (IBA), 150 mmol L^{-1} Tris + Tris, resulting in a pH value of 7.46 and a conductivity of 5810 μS. **P5@NLO** and albumin solution were incubated for 24 h at room temperature prior to FFE studies.

Fluorescence Spectroscopy. Spectra were measured on a multiplate reader (EnSpire Multimode Plate Reader, PerkinElmer, USA). Micelles were analyzed in deionized water. For excitation scans, the emission wavelength was set to 640 nm (**P5-DY654@NLO** and **P5-SH@NLO**), 690 nm (**P5@NLO**), and 700 nm (**P5-MAA$_4$@NLO** and **P5 + P5-MAA$_4$@NLO**). The emission scans were performed by exciting the dye at 480 nm (bandwidth 5 nm). A correction factor was calculated from serial dilutions of the micelles, correcting for differences in NLO loading between micelles. Therefore, the micelles were excited at λ_{Ex} = 488 nm (bandwidth 5 nm), and the emission was measured at λ_{Em} = 575 nm (bandwidth 5 nm). The correction factor represents the relative values of the slope of the fluorescence intensity against the micelle concentration.[63]

Cell Culture. Mouse embryonic fibroblasts were cultured in cell culture flasks at 37 °C, 5% CO_2 (HeraCell CO_2 Incubator, Heraeus, Germany) and water vapor supplemented atmosphere. For the cultivation, Dulbecco's modified Eagle's medium (Gibco, Thermo Fisher Scientific, Germany) supplemented with 10% fetal bovine serum (Thermo Fisher Scientific, Germany), 100 IU streptomycin, 100 IU penicillin (Gibco, Thermo Fisher Scientific, Germany), and 1% stable glutamine (GlutaMax, Gibco, Thermo Fisher Scientific, Germany) was used. Cells were detached and passaged every 3 to 4 days by pipetting.

Cytotoxicity. MEFs were incubated with different micelles in growth media without fetal bovine serum and antibiotics for 24 h. Supernatants were taken, and lactate dehydrogenase (LDH) activity was assessed as a surrogate for membrane damage and toxicity using the CytoTox96 nonradioactive cytotoxicity assay (Promega, Germany). The absorbance of the red formazan product from the conversion of the tetrazolium salt was quantified on a multiplate reader (EnSpire Multimode Plate Reader, PerkinElmer, USA) at 490 nm (bandwidth 5 nm). A 100% cell lysis positive control was used to determine the maximum amount of LDH present. The lysis rate was calculated by subtracting the medium background from each value and relativizing the absorbance values of the treated cells to that of the positive control. Experiments were performed in nine replicates on three individual days.

Micellar Uptake in Murine Embryonic Fibroblasts. Murine embryonic fibroblasts cultivated in 24-well plates as stated above were incubated with various micelles (diluted to a concentration of 10, 100, and 250 μg mL^{-1}) in serum-free medium at 37 °C in a humidified atmosphere. After 24 h, MEFs were detached in PBS (Lonza, Switzerland) containing 5 mmol L^{-1} EDTA (Thermo Fisher Scientific, Germany). The uptake was then quantified using the NLO fluorescence using flow cytometry (BD Accuri C6 Plus, BD Bioscience, Germany) (approximately 10,000 cells per sample). The correction factor was applied to the raw data correcting for the differences in NLO loading, *i.e.*, endogenous brightness between micelles. Experiments were performed in nine replicates on three individual days.

Micellar Uptake Mechanism. MEF cells (4.5 × 10^4 per well) were seeded in 96-well plates and incubated at 37 °C 24 h before the experiment. The medium was then replaced with a serum-free medium containing 30 μmol L^{-1} Pitstop-2 (Sigma-Aldrich, Germany, dissolved in DMSO) or 0.08% DMSO alone and left with cells for 15 min at 37 °C. To check for the energy dependency of the micellar uptake, the cells were incubated with 10 mmol L^{-1} NaN_3 (ATPase-inhibitor)[64] at 37 °C for 1 h or at 4 °C[65] for 1 h before incubation with the micelles, respectively. After incubation, the medium was replaced again with 150 μL of fresh serum-free medium to remove excess Pitstop-2 or NaN_3. To validate the effectiveness of Pitstop-2 in this experiment, we used in parallel nile red (NR)-loaded nanoparticles **P(MMA-*co*-MAA)@NR** (Figure SI15). In a subset of experiments, MEFs were incubated with micelles at 37 and 4 °C for 10 min in DMEM supplemented with 10% fetal bovine serum. These nanoparticles are composed of a statistical copolymer of MMA with 10 mol % of MAA, representing the chemical composition of the micellar core without an OEtOx corona (D_h = 167 nm, PDI 0.08, zeta-potential = −27 mV) and are known for their endocytotic uptake.[56] Micelles (50 μg mL^{-1} in 50 μL of ddH_2O) or polymethacrylate nanoparticle (**P(MMA-*co*-MAA)@NR**), which are known for their endocytosis-dependent uptake, were added for 10 min to the cells. For the temperature-dependent experiment at 4 °C, this step was still at 4 °C. Afterward, cells were detached with PBS (Lonza, Switzerland), 5 mmol L^{-1} EDTA (Thermo Fisher Scientific, Germany) for 30 min at 37 °C in test tubes. The micellar uptake was then quantified utilizing the NLO fluorescence using flow cytometry (BD Accuri C6 Plus, BD Bioscience, Germany). Analysis was performed on 10,000 events per sample. For comparison of the fluorescence intensities, a correction factor was applied. The experiment was performed at least independently three times in duplicates.

Live Cell Imaging. Images were acquired using an LSM-780 microscope (Zeiss AG, Jena, Germany) using a 40× plan-apochromatic air objective (numeric aperture (NA) 0.95) or a plan-apochromatic 63× oil immersion objective (NA 1.40) (both Zeiss AG, Jena, Germany). The plasma membrane of the cells was stained before imaging by incubation of the cells with 5 μg mL^{-1} CellMask Deep Red (Thermo Fisher Scientific, Germany). After 8 min under normal growth conditions, cells were washed twice with prewarmed Hanks' balanced salt solution (HBSS) (Thermo Fisher Scientific, Germany), and FluoroBrite DMEM (Gibco, Thermo Fisher Scientific, Germany) was added. CellMask Deep Red was excited at 633 nm (helium−neon laser) and detected through a 648−744 nm band-pass filter on a photomultiplier tube. Neutral lipid orange (20 nmol L^{-1}) and the different micelles containing NLO at a concentration of 50 μg mL^{-1} were imaged (without additional washing steps) through excitation at 561 nm (helium−neon laser), and fluorescence was detected using a photomultiplier tube through a 571−633 nm band-pass filter for 10 min. The cellular uptake of micelles containing NLO was analyzed using ImageJ 1.51 (Freeware, NIH, USA).[66,67] In brief, the same threshold was applied to all images. The fluorescence

https://doi.org/10.1021/acsnano.1c04213
ACS Nano 2021, 15, 12298−12313

intensity in 15 regions of interest was determined for all images for three independent replicates.

Early Endosome Staining and Micellar Uptake. 7.5×10^4 MEFs per cm^2 were seeded in 4-well chamber slides (μ-slides, ibidi, Munich, Germany). Cells were cultivated for 24 h at 37 °C, 5% CO_2 in DMEM (Gibco, Thermo Fisher Scientific, Germany) supplemented with 10% fetal bovine serum (Thermo Fisher Scientific, Germany), 100 IU streptomycin, 100 IU penicillin (Gibco, Thermo Fisher Scientific, Germany), and 1% stable glutamine (GlutaMaxx, Gibco, Thermo Fisher Scientific, Germany). Afterward, the medium was changed to Opti-MEM (Gibco, Thermo Fisher Scientific, Germany), and 20 particles of Molecular Probes CellLight Early Endosome GFP, BacMam 2.0 (ThermoFischer Scientific, Germany) (Gibco, Thermo Fisher Scientific, Germany) per cell were added and incubated another 18 h at 37 °C, 5% CO_2. Before imaging, cells were washed twice with prewarmed HBSS (Thermo Fisher Scientific, Germany), and FluoroBrite DMEM (Gibco, Thermo Fisher Scientific, Germany) was added. Live cell imaging was then carried out on an LSM-780 (Carl Zeiss AG, Jena, Germany) equipped with a tempered incubation chamber (37 °C) and CO_2 control (5% CO_2). EEA1-GFP was excited at 488 nm (argon laser) and detected through a 493−556 nm band-pass filter on a photomultiplier tube. The different micelles containing NLO were added at a concentration of 50 $\mu g\ mL^{-1}$ and imaged after ∼10 min of incubation (without additional washing steps). NLO was excited at 561 nm (helium−neon laser), and fluorescence was detected using a photomultiplier tube through a 570−753 nm band-pass filter. Images were acquired using a 40× objective and 1.6-fold digital zoom. The pixel size was optimized with respect to the Nyquist criterion for each image. At each position, five *z*-planes were recorded around the brightest focal plane (step size of 0.65 μm). The images were analyzed using the Fiji distribution of ImageJ 1.51 (NIH, USA).[66,67] The *z*-positions were averaged, improving the signal-to-noise ratio and ensuring endosomal structures are fully sampled in all dimensions. Intensities were measured along with line profiles (region of interest, ROI), with each line crossing the center of a GFP-stained endosome. The mean GFP and NLO fluorescence intensity were measured along with the line profile. Five to 10 ROIs were analyzed in each cell. Further, three cells were analyzed per micelle, and the fluorescence intensity was corrected to the cellular background. The plots depict the mean gray value for each channel.

Animals. FVB/N mice (male and female) were used in this study. Animals were maintained at the animal facility of the Jena University Hospital under artificial day−night cycles (12 h light−dark cycles; 23 °C room temperature; 30−60% environment humidity) in a specific pathogen-free environment. Animal studies were conducted following German legislation on the protection of animals and with permission of the Thuringian state administrative office.

***In Vivo* Confocal Laser Scanning Microscopy.** During all procedures and imaging methods, animals remained under deep general anesthesia using 1−2% isoflurane (CP-Pharma, Germany) and 5 $mg\ kg^{-1}$ bodyweight p.o. Meloxicam (0.5 $mg\ mL^{-1}$ suspension, CP-Pharma, Germany) for additional pain relief. Pain reflexes were assessed to gauge the depth of anesthesia. While still under anesthesia, the animals were sacrificed at the end of the experiments. For *in vivo* confocal laser scanning microscopy, first, a tail-vein catheter (30 G) was placed. The liver was exposed by an abdominal incision and carefully placed on a coverslip. Images were acquired using a LSM-780 (Zeiss AG, Jena, Germany) with air-corrected 20× plan-apochromatic (NA 1.15) or 40× plan-apochromatic objective (NA 0.95). Different micelles (∼150 μg) in 5% glucose solution were injected through the tail vein. The NLO cargo fluorescence was illuminated with similar excitation and emission settings as in the *in vitro* experiments. NADPH autofluorescence was employed for hepatocyte detection, as described before.[52] After five areas of interest of each liver were localized, different micelles containing NLO were administered *via* the tail-vein catheter. Then, images were taken every minute to monitor kinetics. Five areas of interest per mouse and ≥3 mice were analyzed. The analysis was done at the time when kinetic analysis showed the highest value in the fluorescence intensity. Image analysis was performed by custom image processing, and the analysis algorithm is described in the next section. Kupffer cells and LSEC staining were performed at the end of the experiment, not to affect the distribution pattern of the micelles. Kupffer cells and LSECs were stained by injection of approximately 10 μg of FITC-labeled F4/80 (clone: BM8) antibody and 6 μg of APC-labeled CD54 (clone: YN1/1.7.4) antibody (Biolegend, USA), respectively. FITC fluorescence illuminated at 488 nm (argon laser) and was detected through a 499−535 nm band-pass filter on a photomultiplier tube.

Image Analysis. Images of labeled and unlabeled liver tissue acquired *via* intravital microscopy were utilized to identify, segment, and quantify various components of the liver using the analysis workflow in Figure SI17. The hepatocytes were identified using label-free techniques[68] based on the autofluorescence images, where their NADPH signal provided proper contrast for a reliable segmentation. In other cases, the end point image of the nanocarrier cargo delivery (cargo: NLO) was used to identify the hepatocytes and to confirm the label-free method (Figures SI17 and SI18A). In the latter case, the precise time sequence tracking of the hepatic cell content of the delivered cargo was only possible with proper precision if the tissue movement during the time sequence imaging was negligible. The canaliculi locations were approximated as the midline between two rows of hepatocytes (Figure SI18A). This approach worked well with autofluorescence-based hepatocyte identification when studying the time dependence of the cargo delivery (supplementary Video SI1). In contrast, the NLO-based approach was able to provide end point information about the final cargo accumulation in the canaliculi, as well as to confirm the label-free localization technique (Figure SI18Ab,Ac). The sinusoids were identified based on the first few frames of the time sequence experiments using the autofluorescence signal. The vessel wall location was later utilized to identify the LSEC, as these cells align themselves with the vessel walls, forming a linear array of bead-shaped small structures. Due to their very characteristic morphology, LSECs were successfully identified throughout the entire time sequence of images by calculating the population-based morphometric and intensity measures (Figure SI18B and supplementary Video SI2). This method provided precise tissue-wide information about the nanocarrier cargo delivery to the LSECs, even though these small cells quickly went in and out of focus during the 2D laser scanning imaging experiments. The resident macrophages of the liver (Kupffer cells) were identified and segmented with high precision based on specific fluorescence labeling applied after the cargo delivery experiments. The Kupffer cells were identified *via* a template-matching algorithm[69] (Figure SI19), where the templates were acquired manually from end point images (Figure SI19A). The template-matched image segments of the Kupffer cells (Figure SI19B) were then preprocessed, binarized using automated thresholding using Otsu's algorithm,[70] and postprocessed to arrive at the close approximation of individual Kupffer cells (Figure SI19C−E). The binary masks were used to calculate the mean fluorescence of the NLO channel (Figure SI19F) in the regions of interest corresponding to each Kupffer cell identified by the binary image segments (Figure SI19G). Finally, the location of the nuclei and the intercellular space was determined based on the low signal regions of the autofluorescence images (supplementary Video SI3). All image analysis tasks were carried out by two custom-written macros (supplementary Video SI4 and Video SI5) using the Fiji distribution of ImageJ 1.52p.[66,67]

Quantitative data were normalized to differences in the intrinsic brightness of the micelles using the correction factor[63] and by the area under the curve calculated from the plasma disappearance rate in large veins (portal veins) of the liver, accounting for differences in the absolute accumulation of the various micelles in the liver. Data were processed with the R open source version 3.5.2 (2018-12-20, "Eggshell Igloo") and R-Studio open source, version 1.1.463. The packages and functions used were the following: *tidyverse*, *stringr*, *purrr*, *dplyr*, *concatenate*, *RMisc*, *readr*, *readxl*. Data are plotted with OriginPro 2019 (OriginLab Corporation).

https://doi.org/10.1021/acsnano.1c04213
ACS Nano 2021, 15, 12298−12313

ASSOCIATED CONTENT

Supporting Information

The Supporting Information is available free of charge at https://pubs.acs.org/doi/10.1021/acsnano.1c04213.

Schematic representation of the detailed synthesis route toward the PMMA-*graft*-OEtOx$_{15}$ graft copolymers; overlay of SEC elugrams for **P5** and **P5-SH** and **P5-SH** with RI and DA detection; SEC elugram, absorption spectrum, emission spectrum, and 3D-SEC elugram of **P5-DY654**; overlay of SEC elugrams of **P5** and **P5-MAA$_4$**; titration investigation of **P5-MAA$_4$**; DLS correlograms; cryo-TEM images and DLS of **P5-MAA$_4$**, **P5-DY654**, and **P5-SH**; general workflow for the determination of the dye uptake; dye uptake results for **P5@NLO** and **P5-MAA$_4$@NLO** and corresponding calibration data; fluorescence excitation and emission of different micelles; Raman mean intensity spectra of different micelles, the neat material, and pure dyes NLO and DY654; principal component (PC-1, PC-2, PC-3) analysis of the Raman spectra; additional discussion of micelle stability; stability of **P5@NLO** investigated by analytical ultracentrifugation; stability of **P5@NLO** in physiologically relevant buffers determined by DLS; stability of **P5@NLO** against albumin determined by FFE; toxicity and uptake in MEF (24 h); uptake of **P(MMA-*co*-MAA)@NR** in the presence of different inhibitors determined by flow cytometry after 10 min incubation; early endosome staining and micellar uptake *in vitro*; flowchart of the automated image processing; identification of canaliculi and LSECs in live liver tissue; identification of the Kupffer cells in live liver tissue; AUC calculated from plasma disappearance; complete description of 6 supporting videos (PDF)

Video S1: Identification of canaliculi (MP4)

Video S2: Segmentation of LSECs *via* population sampling (MP4)

Video S3: Location of hepatocyte nuclei and intercellular space (MP4)

Video S4: Real-time screen capture of the leading image analysis (MP4)

Video S5: Reat-time screen capture of the second image analysis program (MP4)

Video S6: Representation time series (MP4)

AUTHOR INFORMATION

Corresponding Authors

Ulrich S. Schubert − *Laboratory of Organic and Macromolecular Chemistry (IOMC), Friedrich Schiller University Jena, 07743 Jena, Germany; Jena Center for Soft Matter (JCSM), Friedrich Schiller University Jena, 07743 Jena, Germany;* orcid.org/0000-0003-4978-4670; Email: ulrich.schubert@uni-jena.de

Adrian T. Press − *Department of Anesthesiology and Intensive Care Medicine, Jena University Hospital, 07747 Jena, Germany; Medical Faculty, Friedrich Schiller University Jena, 07743 Jena, Germany;* orcid.org/0000-0002-6089-6764; Email: adrian.press@med.uni-jena.de

Authors

⊗**Irina Muljajew** − *Laboratory of Organic and Macromolecular Chemistry (IOMC), Friedrich Schiller University Jena, 07743 Jena, Germany; Jena Center for Soft Matter (JCSM), Friedrich Schiller University Jena, 07743 Jena, Germany*

⊗**Sophie Huschke** − *Department of Anesthesiology and Intensive Care Medicine, Jena University Hospital, 07747 Jena, Germany*

Anuradha Ramoji − *Institute for Physical Chemistry (IPC) and Abbe Center of Photonics (ACP), Friedrich Schiller University Jena, 07745 Jena, Germany; Leibniz Institute of Photonic Technology (IPHT) Jena, Member of the Leibniz Research Alliance - Leibniz Health Technologies, 07745 Jena, Germany;* orcid.org/0000-0003-2723-6614

Zoltán Cseresnyés − *Research Group Applied Systems Biology, Leibniz Institute for Natural Product Research and Infection Biology, Hans Knoell Institute Jena, 07745 Jena, Germany*

Stephanie Hoeppener − *Laboratory of Organic and Macromolecular Chemistry (IOMC), Friedrich Schiller University Jena, 07743 Jena, Germany; Jena Center for Soft Matter (JCSM), Friedrich Schiller University Jena, 07743 Jena, Germany;* orcid.org/0000-0002-5770-5197

Ivo Nischang − *Laboratory of Organic and Macromolecular Chemistry (IOMC), Friedrich Schiller University Jena, 07743 Jena, Germany; Jena Center for Soft Matter (JCSM), Friedrich Schiller University Jena, 07743 Jena, Germany;* orcid.org/0000-0001-6182-5215

Wanling Foo − *Department of Anesthesiology and Intensive Care Medicine, Jena University Hospital, 07747 Jena, Germany*

Jürgen Popp − *Institute for Physical Chemistry (IPC) and Abbe Center of Photonics (ACP), Friedrich Schiller University Jena, 07745 Jena, Germany; Leibniz Institute of Photonic Technology (IPHT) Jena, Member of the Leibniz Research Alliance - Leibniz Health Technologies, 07745 Jena, Germany;* orcid.org/0000-0003-4257-593X

Marc Thilo Figge − *Research Group Applied Systems Biology, Leibniz Institute for Natural Product Research and Infection Biology, Hans Knoell Institute Jena, 07745 Jena, Germany; Institute of Microbiology, Faculty of Biological Sciences, Friedrich Schiller University Jena, 07743 Jena, Germany*

Christine Weber − *Laboratory of Organic and Macromolecular Chemistry (IOMC), Friedrich Schiller University Jena, 07743 Jena, Germany; Jena Center for Soft Matter (JCSM), Friedrich Schiller University Jena, 07743 Jena, Germany;* orcid.org/0000-0003-0712-5255

Michael Bauer − *Department of Anesthesiology and Intensive Care Medicine, Jena University Hospital, 07747 Jena, Germany*

Complete contact information is available at: https://pubs.acs.org/10.1021/acsnano.1c04213

Author Contributions

I.M. planned, synthesized, formulated, and analyzed polymers and micelles. S.Hu. planned, performed, and analyzed *in vitro* and *in vivo* experiments. A.R. planned, performed, and analyzed Raman microspectroscopic analysis. Z.C. planned and conducted image analysis. S.Ho. performed and analyzed cryo-TEM. I.N. planned and performed analytical ultracentrifugation analysis. W.F. established, performed, and analyzed intravital co-staining. M.T.F. supervised the image analysis. J.P. supervised Raman microspectroscopy. C.W. planned the study and supervised the synthesis and analysis. M.B. guided the study and supervised animal experiments.

https://doi.org/10.1021/acsnano.1c04213
ACS Nano 2021, 15, 12298−12313

U.S.S. guided the study and supervised the polymer synthesis and micelle preparation. A.T.P. planned and guided the study, performed animal experiments, and supervised cell experiments and analysis. All authors contributed to writing the manuscript.

Notes

The authors declare no competing financial interest.
[⊗]I.M. and S.H. contributed equally.

ACKNOWLEDGMENTS

This work was funded by the Deutsche Forschungsgemeinschaft (DFG, German Research Foundation), Project No. 316213987 − SFB 1278 (Projects A01, C01, C03, Z01). The cryo-TEM facilities of the Jena Center for Soft Matter (JCSM) were established with a grant from the DFG and the European Funds for Regional Development (EFRE). This work was as well supported by the "Thüringer Aufbaubank (TAB)" and the "Europäischer Fond für regionale Entwicklung (EFRE)" (2018FGI0025) for funding of analytical ultracentrifugation facilities at the JCSM. The authors thank Pelin Sungur (Friedrich Schiller University, Jena) for her technical support on the cryo-TEM. Mouse embryonic fibroblasts were a gift of the Institute of Human Genetics, Jena University Hospital. Dyomics GmbH Jena provided DY654 and neutral lipid orange. The authors would also like to thank Jens Ulbrich for providing the poly(methyl methacrylate), and Dr. Robert Wildgruber and Markart Meckel from the FFE Service GmbH for free flow electrophoresis measurements.

REFERENCES

(1) Villaverde, G.; Baeza, A. Targeting Strategies for Improving the Efficacy of Nanomedicine in Oncology. *Beilstein J. Nanotechnol.* **2019**, *10*, 168−181.
(2) Morachis, J. M.; Mahmoud, E. A.; Almutairi, A. Physical and Chemical Strategies for Therapeutic Delivery by Using Polymeric Nanoparticles. *Pharmacol. Rev.* **2012**, *64*, 505−519.
(3) Cabral, H.; Matsumoto, Y.; Mizuno, K.; Chen, Q.; Murakami, M.; Kimura, M.; Terada, Y.; Kano, M. R.; Miyazono, K.; Uesaka, M.; Nishiyama, N.; Kataoka, K. Accumulation of Sub-100 Nm Polymeric Micelles in Poorly Permeable Tumours Depends on Size. *Nat. Nanotechnol.* **2011**, *6*, 815−823.
(4) Kao, Y. J.; Juliano, R. L. Interactions of Liposomes with the Reticuloendothelial System. Effects of Reticuloendothelial Blockade on the Clearance of Large Unilamellar Vesicles. *Biochim. Biophys. Acta, Gen. Subj.* **1981**, *677*, 453−461.
(5) Zolnik, B. S.; González-Fernández, A.; Sadrieh, N.; Dobrovolskaia, M. A. Nanoparticles and the Immune System. *Endocrinology* **2010**, *151*, 458−465.
(6) Papahadjopoulos, D.; Allen, T. M.; Gabizon, A.; Mayhew, E.; Matthay, K.; Huang, S. K.; Lee, K. D.; Woodle, M. C.; Lasic, D. D.; Redemann, C. Sterically Stabilized Liposomes: Improvements in Pharmacokinetics and Antitumor Therapeutic Efficacy. *Proc. Natl. Acad. Sci. U. S. A.* **1991**, *88*, 11460−11464.
(7) Storm, G.; Belliot, S. O.; Daemen, T.; Lasic, D. D. Surface Modification of Nanoparticles to Oppose Uptake by the Mononuclear Phagocyte System. *Adv. Drug Deliv. Rev.* **1995**, *17*, 31−48.
(8) D'souza, A. A.; Shegokar, R. Polyethylene Glycol (PEG): A Versatile Polymer for Pharmaceutical Applications. *Expert Opin. Drug Deliv.* **2016**, *13*, 1257−1275.
(9) Torchilin, V. P. Polymer-Coated Long-Circulating Microparticulate Pharmaceuticals. *J. Microencapsulation* **1998**, *15*, 1−19.
(10) Veronese, F. M.; Pasut, G. PEGylation, Successful Approach to Drug Delivery. *Drug Discov. Today* **2005**, *10*, 1451−1458.
(11) Yang, Q.; Jacobs, T. M.; McCallen, J. D.; Moore, D. T.; Huckaby, J. T.; Edelstein, J. N.; Lai, S. K. Analysis of Pre-Existing IgG and IgM Antibodies against Polyethylene Glycol (PEG) in the General Population. *Anal. Chem.* **2016**, *88*, 11804−11812.
(12) Chen, B.-M.; Su, Y.-C.; Chang, C.-J.; Burnouf, P.-A.; Chuang, K.-H.; Chen, C.-H.; Cheng, T.-L.; Chen, Y.-T.; Wu, J.-Y.; Roffler, S. R. Measurement of Pre-Existing IgG and IgM Antibodies against Polyethylene Glycol in Healthy Individuals. *Anal. Chem.* **2016**, *88*, 10661−10666.
(13) Kozma, G. T.; Mészáros, T.; Vashegyi, I.; Fülöp, T.; Örfi, E.; Dézsi, L.; Rosivall, L.; Bavli, Y.; Urbanics, R.; Mollnes, T. E.; Barenholz, Y.; Szebeni, J. Pseudo-Anaphylaxis to Polyethylene Glycol (PEG)-Coated Liposomes: Roles of Anti-PEG IgM and Complement Activation in a Porcine Model of Human Infusion Reactions. *ACS Nano* **2019**, *13*, 9315−9324.
(14) Guidolin, K.; Zheng, G. Nanomedicines Lost in Translation. *ACS Nano* **2019**, *13*, 13620−13626.
(15) Kierstead, P. H.; Okochi, H.; Venditto, V. J.; Chuong, T. C.; Kivimae, S.; Fréchet, J. M. J.; Szoka, F. C. The Effect of Polymer Backbone Chemistry on the Induction of the Accelerated Blood Clearance in Polymer Modified Liposomes. *J. Control. Release* **2015**, *213*, 1−9.
(16) Woodle, M. C.; Engbers, C. M.; Zalipsky, S. New Amphipatic Polymer-Lipid Conjugates Forming Long-Circulating Reticuloendothelial System-Evading Liposomes. *Bioconjugate Chem.* **1994**, *5*, 493−496.
(17) Moreadith, R. W.; Viegas, T. X. Poly(2-oxazoline) Polymers − Synthesis, Characterization, and Applications in Development of POZ Therapeutics. In *Polymers for Biomedicine: Synthesis, Characterization, and Applications*, 1st ed.; Scholz, C., Eds.; John Wiley & Sons, Inc.: Hoboken, NJ, 2017; pp 51−76.
(18) Danish, 100. Pipeline - Serina Therapeutics; https://serinatherapeutics.com/pipeline/ (accessed June 8, 2020).
(19) Sedlacek, O.; Hoogenboom, R. Drug Delivery Systems Based on Poly(2-Oxazoline)s and Poly(2-Oxazine)s. *Adv. Therap.* **2020**, *3*, 1900168.
(20) Luxenhofer, R.; Han, Y.; Schulz, A.; Tong, J.; He, Z.; Kabanov, A. V.; Jordan, R. Poly(2-Oxazoline)s as Polymer Therapeutics. *Macromol. Rapid Commun.* **2012**, *33*, 1613−1631.
(21) Lu, Y.; Lin, J.; Wang, L.; Zhang, L.; Cai, C. Self-Assembly of Copolymer Micelles: Higher-Level Assembly for Constructing Hierarchical Structure. *Chem. Rev.* **2020**, *120*, 4111−4140.
(22) Maksym-Bębenek, P.; Neugebauer, D. Study on Self-Assembled Well-Defined PEG Graft Copolymers as Efficient Drug-Loaded Nanoparticles for Anti-Inflammatory Therapy. *Macromol. Biosci.* **2015**, *15*, 1616−1624.
(23) Sant, S.; Poulin, S.; Hildgen, P. Effect of Polymer Architecture on Surface Properties, Plasma Protein Adsorption, and Cellular Interactions of Pegylated Nanoparticles. *J. Biomed. Mater. Res., Part A* **2008**, *87*, 885−895.
(24) Rieger, J.; Passirani, C.-P.; Benoit, J.; Van Butsele, K.; Jérôme, R.; Jérôme, C. Synthesis of Amphiphilic Copolymers of Poly(ethylene Oxide) and Poly(ε-Caprolactone) with Different Architectures, and Their Role in the Preparation of Stealthy Nanoparticles. *Adv. Funct. Mater.* **2006**, *16*, 1506−1514.
(25) Bose, A.; Jana, S.; Saha, A.; Mandal, T. K. Amphiphilic Polypeptide-Polyoxazoline Graft Copolymer Conjugate with Tunable Thermoresponsiveness: Synthesis and Self-Assembly into Various Micellar Structures in Aqueous and Nonaqueous Media. *Polymer* **2017**, *110*, 12−24.
(26) Guillerm, B.; Darcos, V.; Lapinte, V.; Monge, S.; Coudane, J.; Robin, J.-J. Synthesis and Evaluation of Triazole-Linked Poly(ε-Caprolactone)-Graft-Poly(2-Methyl-2-Oxazoline) Copolymers as Potential Drug Carriers. *Chem. Commun.* **2012**, *48*, 2879−2881.
(27) Yildirim, I.; Bus, T.; Sahn, M.; Yildirim, T.; Kalden, D.; Hoeppener, S.; Traeger, A.; Westerhausen, M.; Weber, C.; Schubert, U. S. Fluorescent Amphiphilic Heterografted Comb Polymers Comprising Biocompatible PLA and PEtOx Side Chains. *Polym. Chem.* **2016**, *7*, 6064−6074.
(28) Jana, S.; Bose, A.; Saha, A.; Mandal, T. K. Photocleavable and Tunable Thermoresponsive Amphiphilic Random Copolymer: Self-

https://doi.org/10.1021/acsnano.1c04213
ACS Nano 2021, 15, 12298−12313

Assembly into Micelles, Dye Encapsulation, and Triggered Release. *J. Polym. Sci., Part A: Polym. Chem.* **2017**, *55*, 1714−1729.
(29) Jana, S.; Saha, A.; Paira, T. K.; Mandal, T. K. Synthesis and Self-Aggregation of Poly(2-Ethyl-2-Oxazoline)-Based Photocleavable Block Copolymer: Micelle, Compound Micelle, Reverse Micelle, and Dye Encapsulation/Release. *J. Phys. Chem. B* **2016**, *120*, 813−824.
(30) Korchia, L.; Lapinte, V.; Travelet, C.; Borsali, R.; Robin, J.-J.; Bouilhac, C. UV-Responsive Amphiphilic Graft Copolymers Based on Coumarin and Polyoxazoline. *Soft Matter* **2017**, *13*, 4507−4519.
(31) Oudin, A.; Chauvin, J.; Gibot, L.; Rols, M.-P.; Balor, S.; Goudounèche, D.; Payré, B.; Lonetti, B.; Vicendo, P.; Mingotaud, A.-F.; Lapinte, V. Amphiphilic Polymers Based on Polyoxazoline as Relevant Nanovectors for Photodynamic Therapy. *J. Mater. Chem. B* **2019**, *7*, 4973−4982.
(32) Alvaradejo, G. G.; Nguyen, H. V.-T.; Harvey, P.; Gallagher, N. M.; Le, D.; Ottaviani, M. F.; Jasanoff, A.; Delaittre, G.; Johnson, J. A. Polyoxazoline-Based Bottlebrush and Brush-Arm Star Polymers *via* ROMP: Syntheses and Applications as Organic Radical Contrast Agents. *ACS Macro Lett.* **2019**, *8*, 473−478.
(33) Yamamoto, Y.; Nagasaki, Y.; Kato, Y.; Sugiyama, Y.; Kataoka, K. Long-Circulating Poly(ethylene Glycol)−poly(d,l-Lactide) Block Copolymer Micelles with Modulated Surface Charge. *J. Control. Release* **2001**, *77*, 27−38.
(34) Xiao, K.; Li, Y.; Luo, J.; Lee, J. S.; Xiao, W.; Gonik, A. M.; Agarwal, R. G.; Lam, K. S. The Effect of Surface Charge on *in Vivo* Biodistribution of PEG-Oligocholic Acid Based Micellar Nanoparticles. *Biomaterials* **2011**, *32*, 3435−3446.
(35) Maksym, P.; Neugebauer, D. Synthesis of Amphiphilic Semigrafted Pseudo-Pluronics for Self-Assemblies Carrying Indomethacin. *RSC Adv.* **2016**, *6*, 88444−88452.
(36) Muljajew, I.; Weber, C.; Nischang, I.; Schubert, U. PMMA-G-OEtOx Graft Copolymers: Influence of Grafting Degree and Side Chain Length on the Conformation in Aqueous Solution. *Materials* **2018**, *11*, 528.
(37) Press, A. T; Ramoji, A.; vd Luhe, M.; Rinkenauer, A. C; Hoff, J.; Butans, M.; Rossel, C.; Pietsch, C.; Neugebauer, U.; Schacher, F. H; Bauer, M. Cargo−Carrier Interactions Significantly Contribute to Micellar Conformation and Biodistribution. *NPG Asia Mater.* **2017**, *9*, e444.
(38) Recouvreux, M. V.; Commisso, C. Macropinocytosis: A Metabolic Adaptation to Nutrient Stress in Cancer. *Front. Endocrinol. (Lausanne, Switz.)* **2017**, *8*, 261.
(39) Qiu, L. Q.; Lai, W. S.; Stumpo, D. J.; Blackshear, P. J. Mouse Embryonic Fibroblast Cell Culture and Stimulation. *Bio-protocol* **2016**, *6*, No. e1859.
(40) Dutta, D.; Williamson, C. D.; Cole, N. B.; Donaldson, J. G. Pitstop 2 Is a Potent Inhibitor of Clathrin-Independent Endocytosis. *PLoS One* **2012**, *7*, No. e45799.
(41) Liashkovich, I.; Pasrednik, D.; Prystopiuk, V.; Rosso, G.; Oberleithner, H.; Shahin, V. Clathrin Inhibitor Pitstop-2 Disrupts the Nuclear Pore Complex Permeability Barrier. *Sci. Rep.* **2015**, *5*, 9994.
(42) Sahay, G.; Querbes, W.; Alabi, C.; Eltoukhy, A.; Sarkar, S.; Zurenko, C.; Karagiannis, E.; Love, K.; Chen, D.; Zoncu, R.; Buganim, Y.; Schroeder, A.; Langer, R.; Anderson, D. G. Efficiency of siRNA Delivery by Lipid Nanoparticles Is Limited by Endocytic Recycling. *Nat. Biotechnol.* **2013**, *31*, 653−658.
(43) Zhang, Y.-N.; Poon, W.; Tavares, A. J.; McGilvray, I. D.; Chan, W. C. W. Nanoparticle-Liver Interactions: Cellular Uptake and Hepatobiliary Elimination. *J. Control. Release* **2016**, *240*, 332−348.
(44) Alexis, F.; Pridgen, E.; Molnar, L. K.; Farokhzad, O. C. Factors Affecting the Clearance and Biodistribution of Polymeric Nanoparticles. *Mol. Pharmaceutics* **2008**, *5*, 505−515.
(45) Poon, W.; Zhang, Y.-N.; Ouyang, B.; Kingston, B. R.; Wu, J. L. Y.; Wilhelm, S.; Chan, W. C. W. Elimination Pathways of Nanoparticles. *ACS Nano* **2019**, *13*, 5785−5798.
(46) Rogoff, T. M.; Lipsky, P. E. Role of the Kupffer Cells in Local and Systemic Immune Responses. *Gastroenterology* **1981**, *80*, 854−860.
(47) Sadauskas, E.; Wallin, H.; Stoltenberg, M.; Vogel, U.; Doering, P.; Larsen, A.; Danscher, G. Kupffer Cells Are Central in the Removal of Nanoparticles from the Organism. Part. *Part. Fibre Toxicol.* **2007**, *4*, 10.
(48) Walkey, C. D.; Olsen, J. B.; Guo, H.; Emili, A.; Chan, W. C. W. Nanoparticle Size and Surface Chemistry Determine Serum Protein Adsorption and Macrophage Uptake. *J. Am. Chem. Soc.* **2012**, *134*, 2139−2147.
(49) Poisson, J.; Lemoinne, S.; Boulanger, C.; Durand, F.; Moreau, R.; Valla, D.; Rautou, P.-E. Liver Sinusoidal Endothelial Cells: Physiology and Role in Liver Diseases. *J. Hepatol.* **2017**, *66*, 212−227.
(50) Sørensen, K. K.; McCourt, P.; Berg, T.; Crossley, C.; Le Couteur, D.; Wake, K.; Smedsrød, B. The Scavenger Endothelial Cell: A New Player in Homeostasis and Immunity. *Am. J. Physiol.* **2012**, *303*, R1217−R1230.
(51) Press, A. T.; Traeger, A.; Pietsch, C.; Mosig, A.; Wagner, M.; Clemens, M. G.; Jbeily, N.; Koch, N.; Gottschaldt, M.; Bézière, N.; Ermolayev, V.; Ntziachristos, V.; Popp, J.; Kessels, M. M.; Qualmann, B.; Schubert, U. S.; Bauer, M. Cell Type-Specific Delivery of Short Interfering RNAs by Dye-Functionalised Theranostic Nanoparticles. *Nat. Commun.* **2014**, *5*, 5565.
(52) Halamoda-Kenzaoui, B.; Bremer-Hoffmann, S. Main Trends of Immune Effects Triggered by Nanomedicines in Preclinical Studies. *Int. J. Nanomed.* **2018**, *13*, 5419−5431.
(53) Campbell, F.; Bos, F. L.; Sieber, S.; Arias-Alpizar, G.; Koch, B. E.; Huwyler, J.; Kros, A.; Bussmann, J. Directing Nanoparticle Biodistribution through Evasion and Exploitation of Stab2-Dependent Nanoparticle Uptake. *ACS Nano* **2018**, *12*, 2138−2150.
(54) Vácha, R.; Martinez-Veracoechea, F. J.; Frenkel, D. Intracellular Release of Endocytosed Nanoparticles upon a Change of Ligand-Receptor Interaction. *ACS Nano* **2012**, *6*, 10598−10605.
(55) Fleischer, C. C.; Payne, C. K. Nanoparticle Surface Charge Mediates the Cellular Receptors Used by Protein-Nanoparticle Complexes. *J. Phys. Chem. B* **2012**, *116*, 8901−8907.
(56) Rinkenauer, A. C.; Press, A. T.; Raasch, M.; Pietsch, C.; Schweizer, S.; Schwörer, S.; Rudolph, K. L.; Mosig, A.; Bauer, M.; Traeger, A.; Schubert, U. S. Comparison of the Uptake of Methacrylate-Based Nanoparticles in Static and Dynamic *in Vitro* Systems as Well as *in Vivo*. *J. Control. Release* **2015**, *216*, 158−168.
(57) Schroffenegger, M.; Leitner, N. S.; Morgese, G.; Ramakrishna, S. N.; Willinger, M.; Benetti, E. M.; Reimhult, E. Polymer Topology Determines the Formation of Protein Corona on Core-Shell Nanoparticles. *ACS Nano* **2020**, *14*, 12708−12718.
(58) Corbo, C.; Molinaro, R.; Parodi, A.; Toledano Furman, N. E.; Salvatore, F.; Tasciotti, E. The Impact of Nanoparticle Protein Corona on Cytotoxicity, Immunotoxicity and Target Drug Delivery. *Nanomedicine* **2016**, *11*, 81−100.
(59) Weber, C.; Remzi Becer, C.; Guenther, W.; Hoogenboom, R.; Schubert, U. S. Dual Responsive Methacrylic Acid and Oligo(2-Ethyl-2-Oxazoline) Containing Graft Copolymers. *Macromolecules* **2010**, *43*, 160−167.
(60) Schuck, P.; Rossmanith, P. Determination of the Sedimentation Coefficient Distribution by Least-Squares Boundary Modeling. *Biopolymers* **2000**, *54*, 328−341.
(61) Grube, M.; Leiske, M. N.; Schubert, U. S.; Nischang, I. POx as an Alternative to PEG? A Hydrodynamic and Light Scattering Study. *Macromolecules* **2018**, *51*, 1905−1916.
(62) Nischang, I.; Perevyazko, I.; Majdanski, T.; Vitz, J.; Festag, G.; Schubert, U. S. Hydrodynamic Analysis Resolves the Pharmaceutically-Relevant Absolute Molar Mass and Solution Properties of Synthetic Poly(ethylene Glycol)s Created by Varying Initiation Sites. *Anal. Chem.* **2017**, *89*, 1185−1193.
(63) Lerch, S.; Dass, M.; Musyanovych, A.; Landfester, K.; Mailänder, V. Polymeric Nanoparticles of Different Sizes Overcome the Cell Membrane Barrier. *Eur. J. Pharm. Biopharm.* **2013**, *84*, 265−274.
(64) Lee, K. D.; Nir, S.; Papahadjopoulos, D. Quantitative Analysis of Liposome-Cell Interactions in Vitro: Rate Constants of Binding

and Endocytosis with Suspension and Adherent J774 Cells and Human Monocytes. *Biochemistry* **1993**, *32*, 889−899.
(65) Simões, S.; Slepushkin, V.; Düzgünes, N.; Pedroso de Lima, M. C. On the Mechanisms of Internalization and Intracellular Delivery Mediated by pH-Sensitive Liposomes. *Biochim. Biophys. Acta, Biomembr.* **2001**, *1515*, 23−37.
(66) Rueden, C. T.; Schindelin, J.; Hiner, M. C.; DeZonia, B. E.; Walter, A. E.; Arena, E. T.; Eliceiri, K. W. ImageJ2: ImageJ for the Next Generation of Scientific Image Data. *BMC Bioinf.* **2017**, *18*, 529.
(67) Schindelin, J.; Arganda-Carreras, I.; Frise, E.; Kaynig, V.; Longair, M.; Pietzsch, T.; Preibisch, S.; Rueden, C.; Saalfeld, S.; Schmid, B.; Tinevez, J.-Y.; White, D. J.; Hartenstein, V.; Eliceiri, K.; Tomancak, P.; Cardona, A. Fiji: An Open-Source Platform for Biological-Image Analysis. *Nat. Methods* **2012**, *9*, 676−682.
(68) Cseresnyes, Z.; Kraibooj, K.; Figge, M. T. Hessian-Based Quantitative Image Analysis of Host-Pathogen Confrontation Assays. *Cytometry, Part A* **2018**, *93*, 346−356.
(69) Thomas, L. S. V.; Gehrig, J. Multi-Template Matching: A Versatile Tool for Object-Localization in Microscopy Images. *BMC Bioinf.* **2020**, *21*, 44.
(70) Otsu, N. A Threshold Selection Method from Gray-Level Histograms. *IEEE Trans. Syst. Man Cybern. Syst.* **1979**, *9*, 62−66.

https://doi.org/10.1021/acsnano.1c04213
ACS Nano 2021, 15, 12298−12313